INL/RPT-23-73948
Revision 0

Evaluation of Nickel Alloys, Manufactured through Powder Bed Fusion, for Application for Advanced Nuclear Reactors

July 2023

M3CT-23IN1304021 Milestone Report for the Advanced Materials and Manufacturing Technologies

Michael McMurtrey
Michael Moorehead
Michael Mulholland

Idaho National Laboratory

INL/RPT-23-73948
Revision 0

Evaluation of Nickel Alloys, Manufactured through Powder Bed Fusion, for Application for Advanced Nuclear Reactors

M3CT-23IN1304021 Milestone Report for the Advanced Materials and Manufacturing Technologies

Michael McMurtrey
Michael Moorehead
Michael Mulholland

July 2023

Idaho National Laboratory
Idaho Falls, Idaho 83415

http://www.inl.gov

Prepared for the
U.S. Department of Energy
Office of Nuclear Energy
Under DOE Idaho Operations Office
Contract DE-AC07-05ID14517

Page intentionally left blank

ABSTRACT

In collaboration with other laboratories, Idaho National Laboratory has investigated additively manufactured alloys for applications in advanced nuclear reactors. The primary focus has been on nickel alloys, as well as “other” alloys, which are alloys not considered steel nor nickel-based alloys, manufactured by laser powder bed fusion. Suitability of investigated alloys were considered against a matrix of properties of interest, developed jointly with the collaborating laboratories. For the nickel alloys, Alloys 282 and 625 are considered promising due to their properties, existing data, and availability of commercial powder feedstock. Haynes 244 is also of interest for its molten salt corrosion resistance, however there is no current feedstock supply chain, and no experience with this alloy as an additively manufactured material. Iron-chrome-aluminum alloys, titanium alloys, zirconium alloys, ceramics, and ceramic inclusions were all considered within the other alloys category. The results and discussions within this report will be compiled with the investigations from the other collaborating laboratories and compiled into a final report later this year (2023).

Page intentionally left blank

ACKNOWLEDGEMENTS

This work was funded under the United States Department of Energy Office of Nuclear Energy Advanced Materials and Manufacturing Technologies Program. EOS Sweden provided additively manufactured Alloy 282 for the preliminary studies discussed within this report, and Haynes International and Special Metals Inc. are acknowledged for their useful discussions on potential nickel alloys of interest for this study. The authors would like to additionally acknowledge Kris Woodbury at Idaho National Laboratory for assistance in encapsulating the additively manufactured Alloy 282 specimens and Sebastien Dryepondt at Oak Ridge National Laboratory for useful discussions on printing nickel alloys, as well as providing material for future studies.

Page intentionally left blank

CONTENTS

FIGURES

TABLES

Page intentionally left blank

ACRONYMS

AM	Additive manufacturing
AMMT	Advanced Materials and Manufacturing Technologies
ANL	Argonne National Laboratory
BSE	Back-scattered electrons
DBTT	Ductile-to-brittle transition temperature
EBSD	Electron back-scattered diffraction
HEA	High entropy alloy
HIP	Hot isostatic press
INL	Idaho National Laboratory
IPF	Inverse pole figure
LPBF	Laser powder bed fusion
ODS	Oxide dispersion strengthened
ORNL	Oak Ridge National Laboratory
PNNL	Pacific Northwest National Laboratory
SEM	Scanning electron microscope
TCP	Topographically close-packed
TS	Tensile strength
YS	Yield strength

Page intentionally left blank

Evaluation of Nickel Alloys, Manufactured through Powder Bed Fusion, for Application for Advanced Nuclear Reactors

1. Introduction

The Advanced Materials and Manufacturing Technologies (AMMT) Program is working to develop cross-cutting technologies that support a broad range of advanced nuclear reactor technologies. The overarching vision of the AMMT Program is to accelerate the development, qualification, demonstration, and deployment of advanced materials and manufacturing technologies to enable reliable and economical nuclear energy. Within the AMMT Program, Idaho National Laboratory (INL) has collaborated with Oak Ridge National Laboratory (ORNL), Pacific Northwest National Laboratory (PNNL), and Argonne National Laboratory (ANL) to identify material candidates for additive manufacturing of interest to a broad range of advanced nuclear reactors and determine their suitability for use with the laser powder bed fusion (LPBF) additive manufacturing (AM). INL's primary focus was on nickel alloys, in partnership with ORNL, and "other" alloys which referrs to non-steel and non-nickel-based alloys, where INL partnered with PNNL to examine potential other alloys of interest to advanced nuclear reactors.

This work focused on understanding potential candidate alloys and down selecting to specific materials that would have significant impacts when fabricated using advanced manufacturing technologies like LPBF. Materials for AM, with a focus on LPBF will be selected by considering their relative importance among the candidate nuclear materials as well as technological readiness levels of the base alloys for possible nuclear applications. The selection process is based on potential impact to the nuclear industry, material processability via AM technologies, and improved performance. The decision matrix was determined collaboratively with INL, ORNL, PNNL, ANL.

The decision matrix was set to include a number of relevant properties meant to describe the feasibility and utility of an alloy for use in nuclear with AM. The matrix was divided into seven categories, which are:

- Manufacturing/Powder
- Manufacturing/Components
- History & Applications
- Mechanical Properties
- Environmental Properties
- Physical Properties
- Microstructure

Each of these categories has several sub-criteria. These will not be covered in detail in this report, nor will scores be assigned values for materials looked at within this report. This will be covered in an upcoming report with the input from all four labs and will be delivered by ORNL later this year (2023). This report will focus on the work performed at INL identifying and evaluating potential printable nickel alloys. It includes literature research as well as the preliminary testing and characterization of material. While nickel alloys are the prime focus of this report, the literature research on potential other alloys is also included.

2. Nickel Alloys

Nickel alloys are of interest to a wide range of advanced reactor designs due to their good high temperature strength and general corrosion resistance. There are concerns, however, that need to be evaluated, with respect to the nickel alloys' printability. Most nickel-based alloys are highly susceptible to cracking during welding (LPBF is essentially a laser-based welding process), including solidification cracking, hot tearing, grain boundary liquation cracking, and strain age cracking due to their wide solidification ranges and high concentrations of segregating and precipitating elements [1, 2]. LPBF parameters must therefore be carefully selected to minimize these defects. Parameters such as scan speed, laser power, and scan path must be optimized to minimize porosity and cracking [3, 4]. Three categories of nickel alloys were identified as potentially of interest to advanced reactor designs:

- Alloys with high temperature strength
- Alloys with low amounts of cobalt
- Alloys with good compatibility with molten salts

All nickel alloys tend to have good high temperature mechanical properties, however, some, such as Alloys 230, 233, 740H, 282, and 617, are particularly optimized for their high temperature strength. This often comes with the inclusion of alloying elements to create strengthening phases. Some of those alloying elements, such as cobalt, are not desirable in applications where they will see neutron irradiation, so a separate class with low cobalt was considered. These alloys, such as Alloys 718, 625, and 800H, tend not to have as good of high temperatures strength, but are more suitable for applications that will receive irradiation (note that nickel in general has concerns with irradiation and helium generation, so there will always be some restrictions on the irradiation application of these alloys). Finally, molten salt, particularly of interest to the molten salt cooled reactor designs, but also of interest for thermal transport or storage in some other reactor designs, can cause significant corrosion in materials. Nickel alloys, particularly Hastelloy N and Alloy 244, tend to resist the molten salt corrosion and are likely to see applications in this environment.

As INL and ORNL are collaborating in investigating nickel alloys, early discussions were centered around a plan to divide the alloys into two groups so that each lab could focus on a more limited set of alloys and to decrease overlap in efforts. INL has focused on Alloys 625, 282, 244, 233, 617, 740H, and a newly developed aerospace material GRX810. By design, both INL and ORNL have been examining Alloy 282, as it is a considered a promising alloy for high temperature energy applications.

Within the Ni-based alloy family, some alloys are more easily printable than others. A given alloy's printability generally depends on its solidification range, gamma prime fraction, phase fraction of topographically close-packed (TCP) phases, and impurity concentrations [2, 5, 6]. Figure 1 [2] shows the strain age cracking propensity plotted against the gamma prime volume fraction, with several of the alloys of interest shown on the figure. The two appear to be linearly related. The alloys of interest for this report are all in the low strain age cracking area. The main alloys of interest will be discussed individually in the following sections. Their nominal compositions are shown in Table 1.

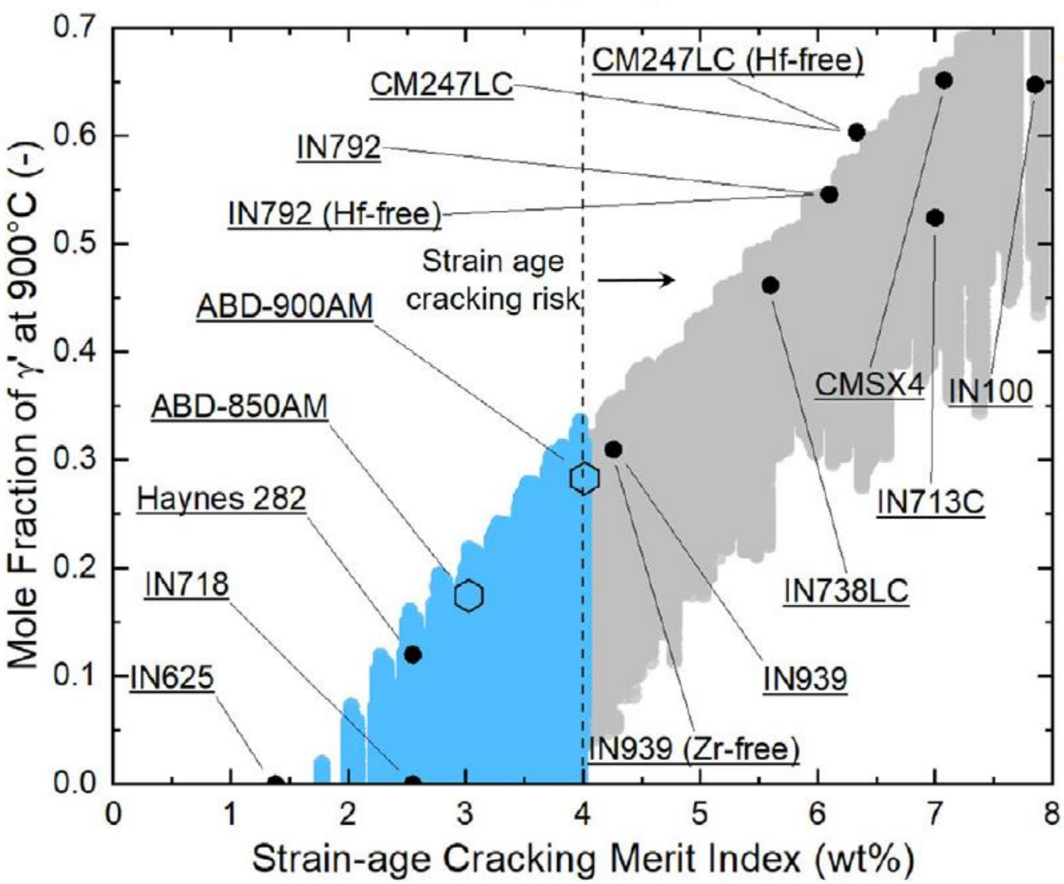

Figure 1. Relationship between gamma prime fraction and strain-age crack merit index.[2]

Table 1. Nominal compositions of alloys of interest (Balanced is shortened to Bal.)

Alloy	H282	740H	IN625	IN617	H244	H233	GRX-810
Cr	20	24.5	22	22	8	19	29
Co	10	20	<1	13		19	33
Mo	8.5	0.1	9	9	22.5	7.5	
Ti	2.1	1.35	<.4	<0.6		0.5	0.25
Al	1.5	1.35	<.4	1	<0.5	3.3	0.3
Fe	<1.5		<5	<3	<2	<1.5	
Mn	<0.3		<.5	<1	<0.8	<0.4	
Si	<0.15	0.15	<.5	<1		<0.2	
C	0.06	0.03	0.05	0.1	<0.03	0.1	0.05
B	0.005			<0.006		0.004	
Ta			1			0.5	
Nb		1.5	3				0.75
W					6	<0.3	3
P			<.015				
S				<.015			
Cu				<0.5			
Y						<0.025	
Zr						0.03	
Re							1.5
Y_2O_3							yes
Ni	Bal.	Bal.	Bal.	Bal.	Bal.	Bal.	Bal.

2.1 Haynes 282

Haynes 282 (H282) is a weldable gamma prime strengthened alloy. H282 was designed for high temperature structural applications, especially gas turbine components [7]. H282 has 10 wt.% Cobalt (Co), which prevents it from being used for in-core components in nuclear power plants. H282 is generally considered to be relatively easy to print, and several authors report finding printing parameters that yielded nearly defect-free builds [8-10]. Haynes 282 powder is licensed to and readily available from multiple suppliers, such as EOS, Hoganas, Praxair, etc.

2.2 Mechanical properties

Mechanical property data on LPBF H282 is available. Room temperature yield strengths (YS) and tensile strengths (TS) have been reported to be around 600 MPa and 900 MPa, respectively in the build direction and as built condition [9, 10]. After aging, the yield and tensile strength in the build direction increase to on the order of ~950 and 1100 MPa, respectively. The tensile strength is stronger than wrought H282[7], which has a listed YS and TS of 715 MPA and 1147 MPa, respectively, though the printed material has a lower ductility. The strength values of LPBF H282 are also reported to have significant anisotropy, which remains after precipitation hardening heat treatment. For example, the horizontal as built YS and TS values are 722 and 1012 MPa [10]. After heat treatment, these values increase to 1000 and 1300 MPa, which is significantly higher than both the build direction properties and the wrought properties. Again, the ductility is correspondingly lower than the wrought value.

The high temperature mechanical properties are of much more interest for Ni-based alloys than the room temperature properties that many LPBF studies tend to focus on. Limited high temperature mechanical property data are available. Shaikh et al [10] report the yield and tensile strength at 800 °C to be 579 and 674 MPa, which is very similar to the values reported by Haynes for wrought material. Christofidou et al [8] reported YS and TS values of 300 and 330 MPa at 927 °C. This is almost identical to the wrought values.

Christofidou et al reported creep-rupture data for LPBF H282 subjected to various heat treatments. For LPBF material that was fully recrystallized and aged according to the standard 2-step heat treatment, they reported ~105 hours to rupture at a load of 120 MPa. Shaikh et al also reported creep stress-rupture data at 927 °C, but their samples were not recrystallized. They found that the stress-rupture performance was highly anisotropic: rupture required 146 h at a stress of 89 MPa while testing in the build direction, but only 45 h in the transverse direction. The anisotropy is similar to the findings of Kunze et al for the superalloy Inconel 738 [11]. The reported rupture time for wrought H282 at 90 MPa of stress is 100 h, which is not as good as the LPBF material results in the build direction but better than the LPBF material in the transverse direction. The anisotropic creep results exhibited by the LPBF material are due to its highly anisotropic grain size in the non-recrystallized state.

2.2.1 Oxidation Resistance and Irradiation Response

Data on the oxidation resistance of LPBF H282 is limited. Romedenne et al [12] found that non-recrystallized LPBF H282 had worse oxidation resistance at 800 and 950 °C than as-cast H282. No investigation has been conducted on the irradiation response of LPBF H282.

2.3 Inconel 625

Inconel 625 (IN625) is a solution-strengthened alloy. IN625 was designed for high temperature structural applications in corrosive environments, such as turbine components, chemical plant components, and nuclear power reactor core components [13]. Since it does not contain Co, it can more readily be used for in-core applications. IN625 was found to be highly printable with a wide processing window by Wong et al. [14]. IN625 powder is widely available from many suppliers.

2.3.1 Mechanical Properties

Many studies of LPBF IN625 focused on the microstructure and room temperature tensile properties. Marchese et al [15] reported the as-built tensile properties in the transverse direction as 783 and 1041 MPa, respectively. Tian et al [16] and Yadriotsev et al. [17] report similar values in the transverse direction. Yadriotsev et al reported that the yield and tensile strength in the build direction is 800 MPa due to the anisotropic as-built microstructure, while the tensile strength is similar to the transverse direction at 1030 MPa. Most authors did not report tensile properties in the build direction. These values are stronger than the rolled and annealed wrought values reported in [13], which are ~530 MPa and 930 MPa.

Limited data exists for high temperature properties of LPBF IN625. Lee et al. [18] reported the high temperature tensile properties at several temperatures and compared them to wrought values. They found that the as-built YS and TS of LPBF IN625 at 700 °C were 520 and 743 MPa, respectively. The fully recrystallized microstructure had yield and tensile strength values of 280 and 615 MPa at 700 °C. Both of these conditions were stronger than the wrought IN625 material at 700 °C, which had a yield strength and tensile strength of 210 and 612 MPa, respectively. Kim et al. [19] reported tensile and fatigue data of hot isostatic pressed (HIP'ed) LPBF IN625 at 650 °C. They found that the YS and TS values were 246 and 637 MPa. The yield strength was similar to the wrought value, but the wrought tensile strength was higher at 721 MPa. Despite undergoing HIP, the LPBF material still had worse fatigue performance than the wrought component in the high cycle fatigue region.

Son et al. [20] studied the creep behavior of LPBF IN625 at 650 and 800 °C. They found that the creep strength of LPBF IN625 was the same or better (in the case of HIP'ed parts) than wrought IN625 at a given strain rate. However, the creep ductility of LPBF parts was significantly inferior to wrought IN625.

2.3.2 Oxidation Resistance and Irradiation Response

A few authors investigated the oxidation resistance of LPBF IN625. Ramenette et al. [21] found that as-built LPBF IN625 had significantly worse oxidation resistance than wrought IN625 at 1050 °C due to the inherent segregation of Mo and Nb to boundaries during the LPBF synthesis. At 900 °C, the oxidation resistance of LPBF IN625 was only slightly worse than that of wrought IN625. Lewis et al. [22] found that heat treating LPBF IN625 at 1177 °C to recrystallize it produced an oxidation resistance at 950 °C that was almost as good as that of the wrought material.

Andurkar et al. and Keya et al. [23, 24] studied the irradiation response of wrought and LPBF IN625 samples under fast neutron irradiation. They found that LPBF IN625 exhibited less irradiation induced hardening than wrought IN625. Andurkar et al. also found that the as-built, build direction samples underwent less irradiation induced hardening than other orientations. Cieslik et al. [25] studied the irradiation response of LPBF and wrought IN625 under ion irradiation. Contrary to the results of Andurkar et al., they found that the LPBF material had a higher hardness change than the wrought material after ion irradiation.

2.4 Inconel 617

Inconel 617 (IN617) is a solution strengthened alloy designed for high temperature strength and oxidation resistance [26]. IN617 contains Co, so it should not be used for in-core applications, but is of interest to some advanced nuclear reactor designs as a secondary heat exchanger material. No data on IN617 parts produced by LPBF is available in the published literature. IN617 powder has limited availability.

2.5 Haynes 244

Haynes 244 (H244) is a precipitation strengthened alloy designed for low thermal expansion engine parts [27]. Due to its low Cr and high Mo concentration, it has potential application in molten salt environments. H244 does not contain Co, so it can be used for in-core applications. No data on H244 parts produced by LPBF is available in the published literature. H244 powder can be made by licensed suppliers but is not generally available off the shelf.

2.6 Haynes 233

Haynes 233 (H233) is a solution and carbide strengthened alloy designed for extreme high temperature oxidation resistance [28]. It can be precipitation strengthened at intermediate temperatures. Since it has a significant Co addition, it should not be used for in-core applications. No data on H233 parts produced by LPBF is available in the published literature. H233 powder can be made by licensed suppliers but is not generally available off the shelf.

2.7 Inconel 740H

Special Metals Inconel 740H (IN740H) is a precipitation strengthened alloy designed for corrosion resistance in high temperature coal power plants [29]. IN740H contains Co, so it should not be used for in-core applications. No data on IN740H parts produced by LPBF is available in the published literature. IN740H powder is not generally available off the shelf.

2.8 GRX-810

GRX810 is an oxide dispersion strengthened (ODS), high Co medium entropy Ni-based alloy invented by NASA [30] as a printed nickel alloy for very high temperature service at temperatures > 810 °C. Since it contains Co, it cannot be used for in-core applications. GRX-810 powder is not yet available from any commercial suppliers. It requires a specialized mixing step to incorporate Y2O3 dispersoids into the metal powder [30].

2.8.1 Mechanical Properties

The high temperature creep performance of GRX-810 has been studied by Smith et al. [30]. GRX-810 produced by LPBF and post-HIP was found to have a 1000 h creep rupture strength of ~35 MPa at 1093 °C. The high temperature TS of as-built GRX-810 was found to be ~130 MPa at 1093 °C, while the HIP'ed sample had a TS of ~120 MPa at 1093 °C.

2.8.2 Oxidation Resistance and Irradiation Response

LPBF GRX-810 was found to have superior oxidation resistance to IN718 at 1093 °C and 1200 °C. It lost ~0.1 g/cm2 after 5 h at 1200 °C, while IN718 failed catastrophically. No data is available on the irradiation response of GRX-810.

2.9 Nickel Alloys Comparisons

2.9.1 1.6.1 High temperature mechanical properties

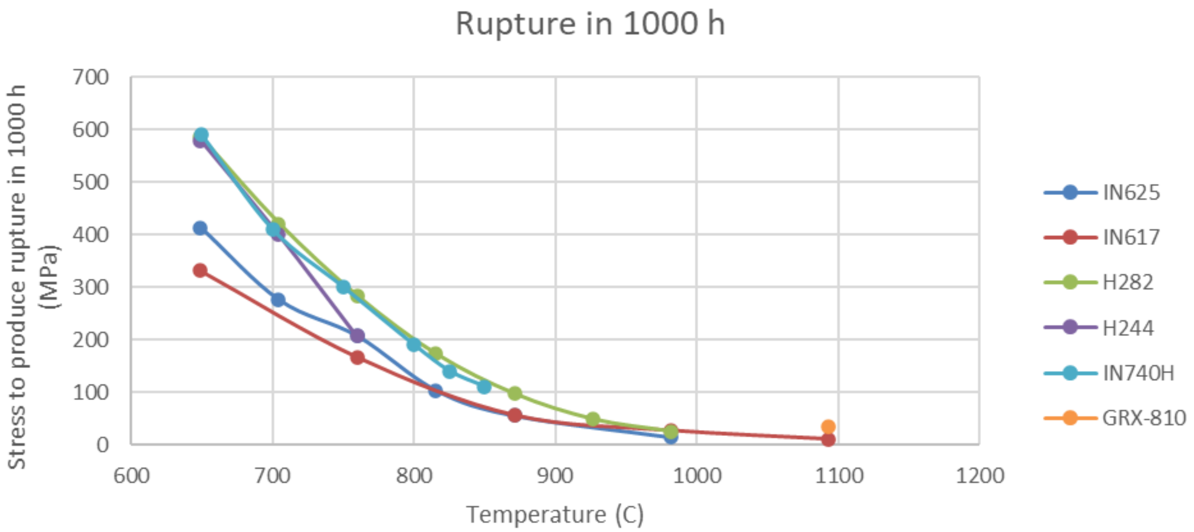

Figure 2. Creep stress-rupture data for alloys of interest. Data taken from [7, 13, 26, 27, 29, 30]

Because most alloys studied do not have sufficient high temperature mechanical property data for samples manufactured by LPBF, a comparison can be made using the published wrought properties. Figure 2 shows the wrought stress-rupture data taken from the manufacturer brochures [7, 13, 26, 27, 29, 30] for the alloys studied. H233 does not have sufficient data to add to the figure. It can be seen that the precipitation strengthened alloys IN740H, H282, and H244 have higher creep rupture strengths than the solution strengthened alloys in the temperature range of 650-760 °C. At 760 °C, the ɣ" precipitation in H244 apparently coarsens and/or dissolves, reducing its strength to the same level as IN625. At temperatures above 927 °C, the gamma prime precipitation in IN740H and H282 dissolves, reducing their strength levels to that of the solution strengthened alloys. GRX-810 appears to have higher creep-rupture strength than IN617 at high temperatures due to its ODS component.

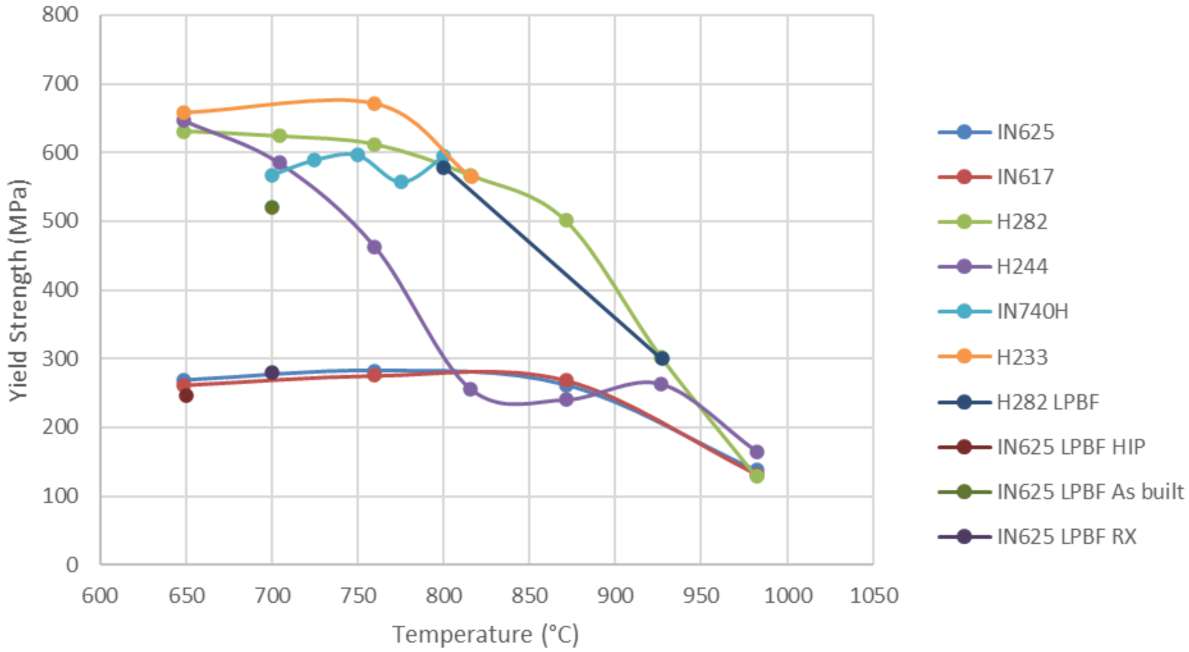

Figure 3. High temperature yield strength of selected alloys. Data from [7, 10, 13, 18, 19, 26-29].

Figure 3 shows a comparison of high temperature YS data from both wrought alloys and the LPBF data that is available [7, 10, 13, 18, 19, 26-29]. Again, the precipitation strengthened alloys have higher strengths than the solution strengthened alloys over most of the temperature range. At the highest temperatures, the YS of all alloys are very similar. As stated above, the high temperature YS values of the alloys made by LPBF are very similar to or in some cases better than those of the wrought alloys.

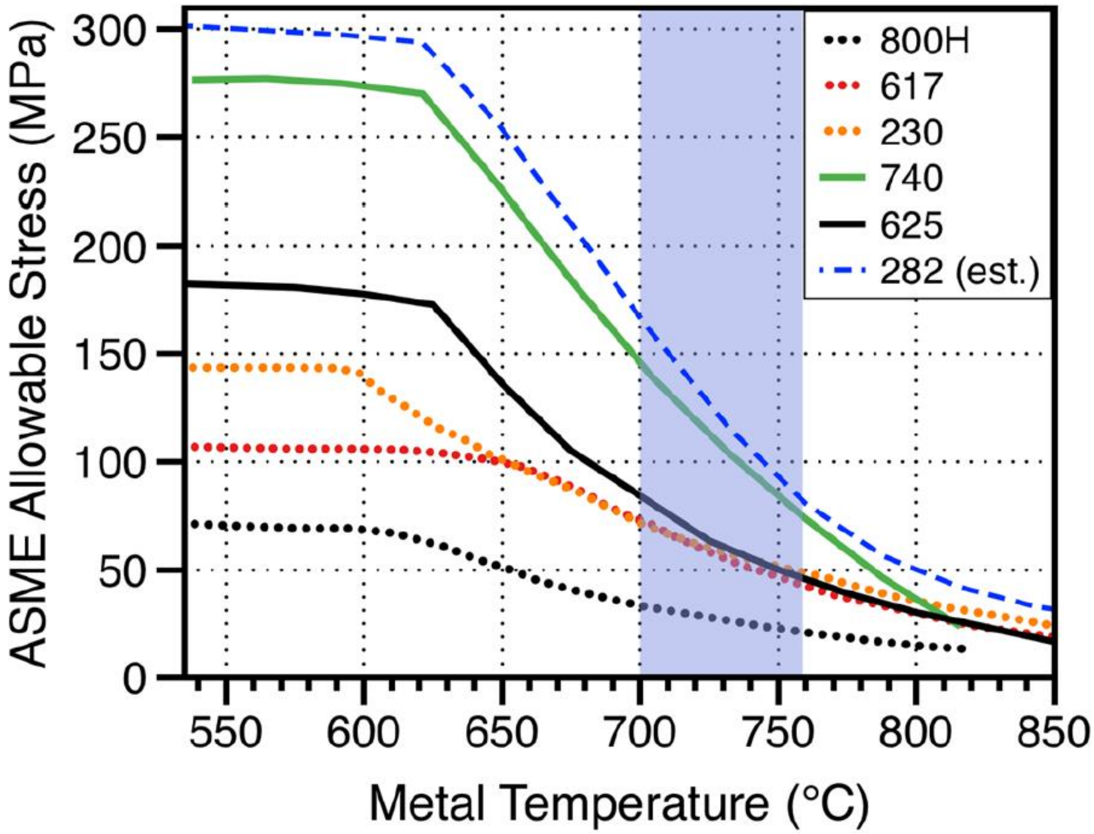

Figure 4. ASME allowable stress as a function of temperature for various nickel-based alloys.[31]

Figure 4 [31] shows a comparison of maximum allowable stress as per the ASME Boiler and Pressure Vessel Code as a function of temperature for various wrought Ni-based alloys. The allowable stress follows the trends shown in Figure 2 and Figure 3, as expected.

2.9.2 Powder Availability

Of the alloys studied, IN625 has the highest availability from the most suppliers, followed by H282, which is still available off-the shelf from many suppliers. Most of the other alloys are available as custom batches from a few select suppliers, such as Praxair and Hoganas, and so they are much less available than IN625 and H282. GRX-810 is not yet available from any supplier.

2.9.3 Oxidation and Corrosion Resistance

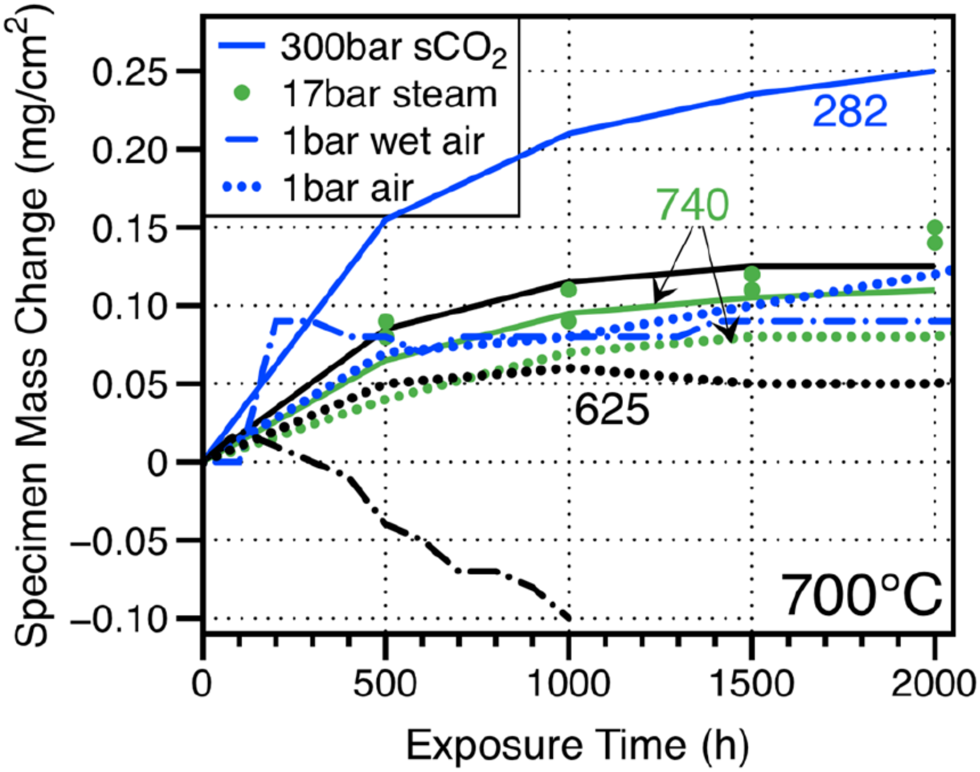

Figure 5. Mass change of various alloys after exposure to various environments. [31]

Figure 5 [31] shows the mass change of IN740, IN625, and H282 as a function of exposure time to four different environments. It is evident that the solution strengthened alloy IN625 has the best oxidation resistance in normal air. IN740 appears to have the best corrosion resistance in sCO_2. H282 appears to be more stable than IN625 in wet air. H282 was also found by Dudziak et al. [32] to gain more mass than IN617 in a steam environment at 700 °C. Based on data in [7, 26-29], it appears that H282 is generally the least resistant to oxidation and steam corrosion. H233 appears to be the most resistant to very high temperature oxidation (> 900 °C). As mentioned above, GRX-810 appears to have superior oxidation resistance to IN718 at high temperatures. It is difficult to compare the oxidation resistance of H233 to that of GRX-810 since the sources do not provide the same type of oxidation data. H244 is slightly more corrosion and oxidation resistant than H282. IN740H is very resistant to corrosion in carbon containing environments such as coal ash [29].

2.9.4 Irradiation response

The irradiation response of most alloys other than IN625 has not been studied much. However, since all the alloys except IN625 and H244 contain significant amounts of cobalt and are not expected to be used for in-core applications, their irradiation response is less relevant.

2.10 Experimental Results from H282 Study

2.10.1 Motivation

The following section details experimental work performed at INL as a part of this program. As stated above for IN625 and H282, the as-built properties of nickel-based alloys manufactured by LPBF are anisotropic due to their anisotropic microstructures. This anisotropy manifests itself in everything from room temperature tensile properties to high temperature creep properties, and is undesirable because it imparts a directional dependence of design stresses for components. One way to reduce the anisotropy of mechanical properties is to heat treat the microstructure. Various authors [8-10] found that the standard wrought solution heat treatment at 1100 °C did not recrystallize the anisotropic microstructure produced by LPBF. A study of the recrystallization kinetics of LPBF H282 is therefore in progress in order to optimize the microstructure and minimize anisotropy. Once this study is completed, high temperature mechanical testing (creep and fatigue, primarily) will be performed to provide additional data on these properties for LPBF material, as there is currently such a limited amount of data that it is difficult to determine the usability of these alloys produced by LPBF.

2.10.2 Materials

EOS Sweden supplied four bars of H282 manufactured by LPBF, with each bar measuring 72x13x13 mm^3. The bars were sectioned in the build and transverse directions to characterize the as-built microstructure. Pieces in both directions were then encapsulated in quartz tubes that were evacuated and partially backfilled with Ar gas to avoid oxidation during heat treatments. The quartz tubes were heat treated in a standard tube furnace under the following conditions: 1250 °C for 1 and 2 h, 1210 °C for 2 h, 1180 °C for 1 h, 1100 °C for 1 h. All samples were furnace cooled after the completion of the heat treatment.

Samples for microstructural examination were mounted and prepared using standard silicon carbide papers and diamond polishing suspensions. Samples for Electron Back-Scattered Diffraction (EBSD) analysis were final polished with 0.01 µm colloidal silica. Samples for optical microscopy were electrolytically etched in 10% oxalic acid at 2.2 V. EBSD was performed on a FEI Quanta field emission gun scanning electron microscope (SEM) using a magnification of 200X, working distance of 14-15 mm, and step size of 0.8-0.9µm.

2.10.3 Results to date

Figure 6 shows an optical micrograph of the as-built H282 samples. In the figure, the build direction is toward the top of the page. Overlapping melt pools are visible, as are elongated columnar grains and areas of cellular microstructure. A small amount of round, gas induced pores are also visible. Figure 7 shows the same sample in the transverse direction. The grain size appears much smaller in this orientation. The laser scanning tracks are visible in this orientation. A small amount of gas porosity and one irregular shaped pore are visible.

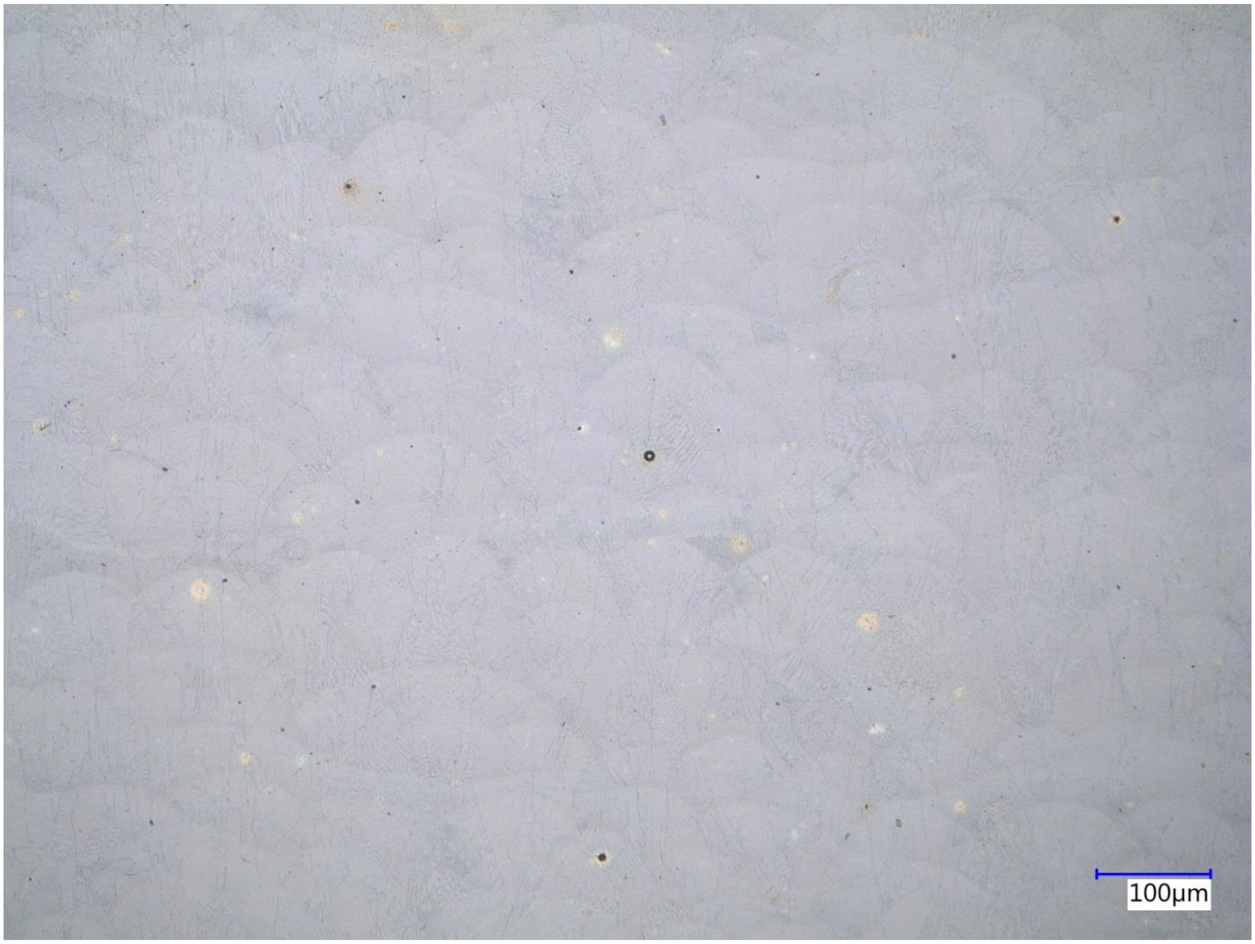

Figure 6. Optical Micrograph of as-built LPBF H282, with the build direction going toward the top of the page in the image. 300X magnification, oxalic acid etch.

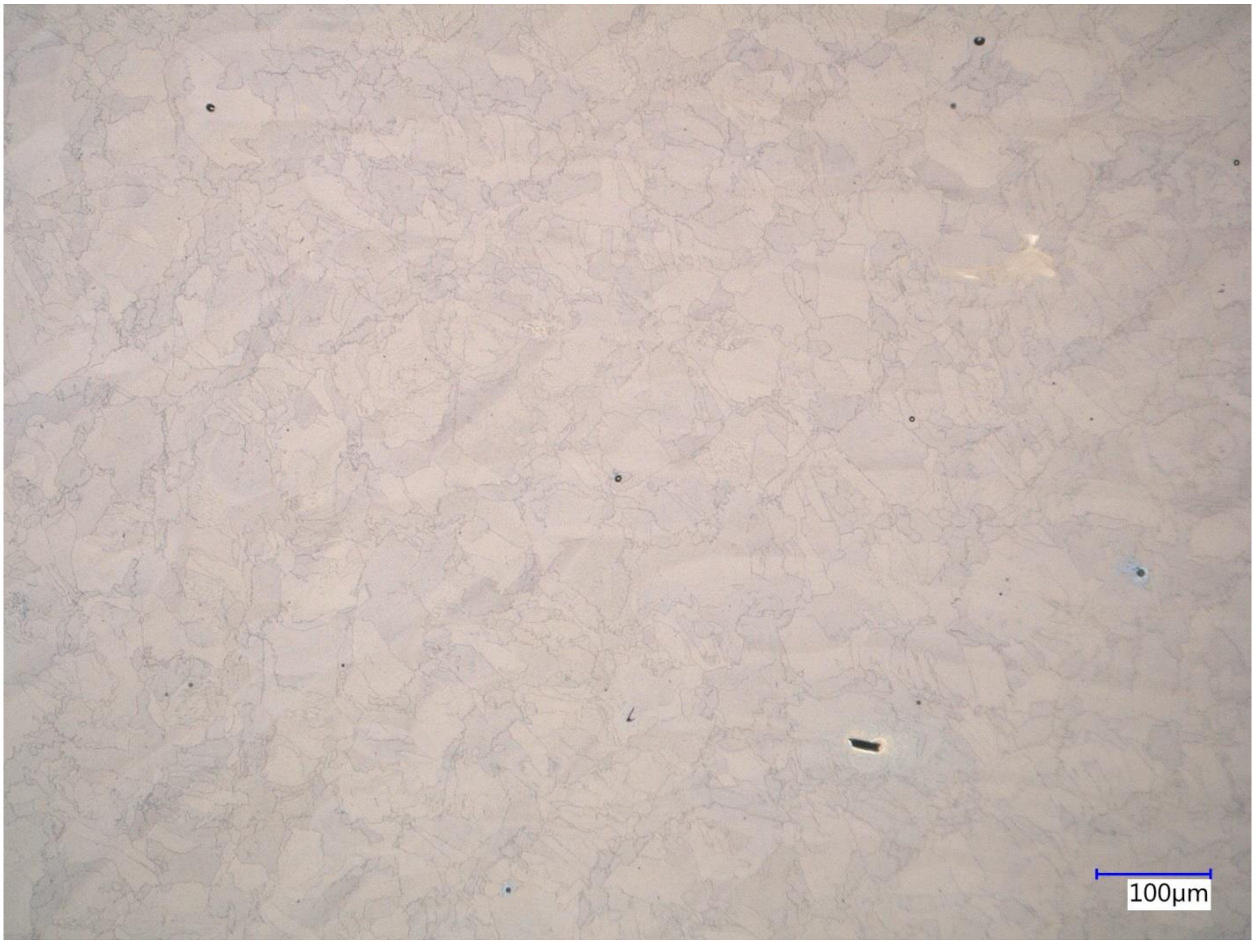

Figure 7. Optical Micrograph of as-built LPBF H282, sectioned in the transverse direction. 300X magnification, oxalic acid etch.

In contrast to the as-built microstructure, Figure 8 shows an optical micrograph of the H282 sample aged at 1210 °C for 2 h. In this case, the grains appear roughly equiaxed and much larger. Annealing twins are also visible.

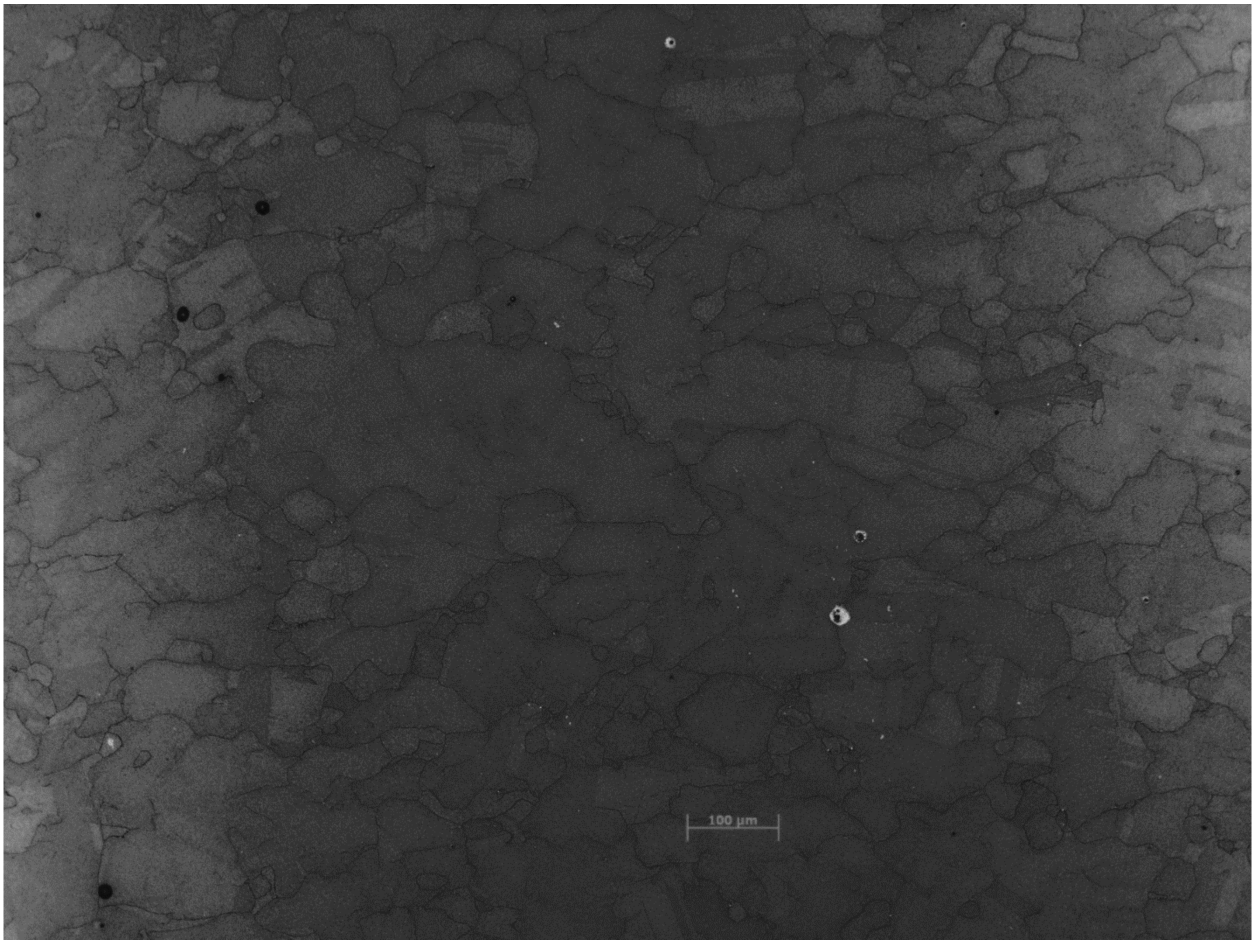

Figure 8. Optical Micrograph of LPBF H282 heat treated at 1210 °C for 2 h, with the build direction going toward the top of the page in the image. 100X magnification, oxalic acid etch.

Figure 9 shows an SEM image of the as-built microstructure using back-scattered electron (BSE) imaging. The elongated grains are visible here. Elemental micro-segregation of elements such as Cr is also evident as variations in the gray scale intensity of the image. Cellular microstructure is evident in Figure 9. A higher magnification image of an area of cellular microstructure is also displayed in Figure 10. To more accurately quantify the grain size, EBSD analysis was performed on the various samples. Figure 11 shows an EBSD inverse pole figure (IPF) map of the as built H282.

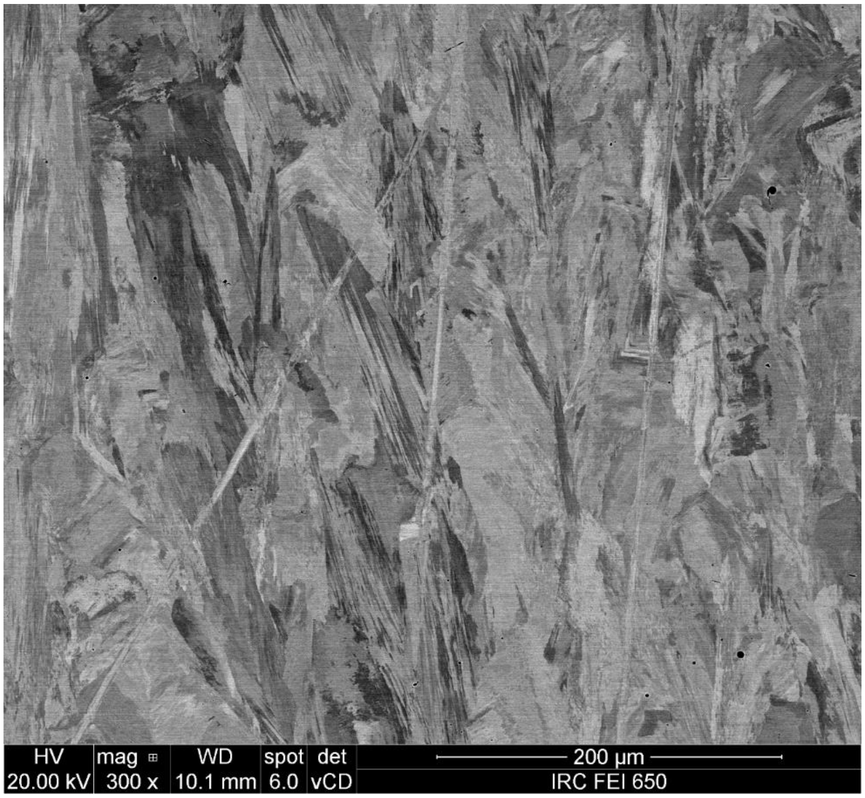

Figure 9. SEM BSE image of as built LPBF H282, with the build direction going toward the top of the page.

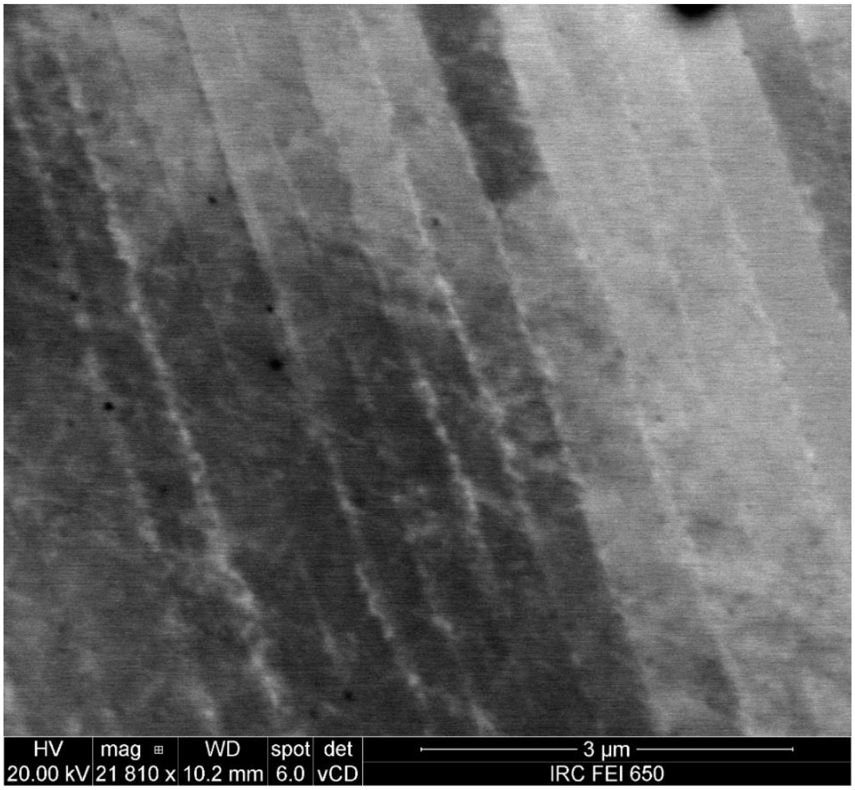

Figure 10. Higher magnification SEM BSE image of cellular microstructure.

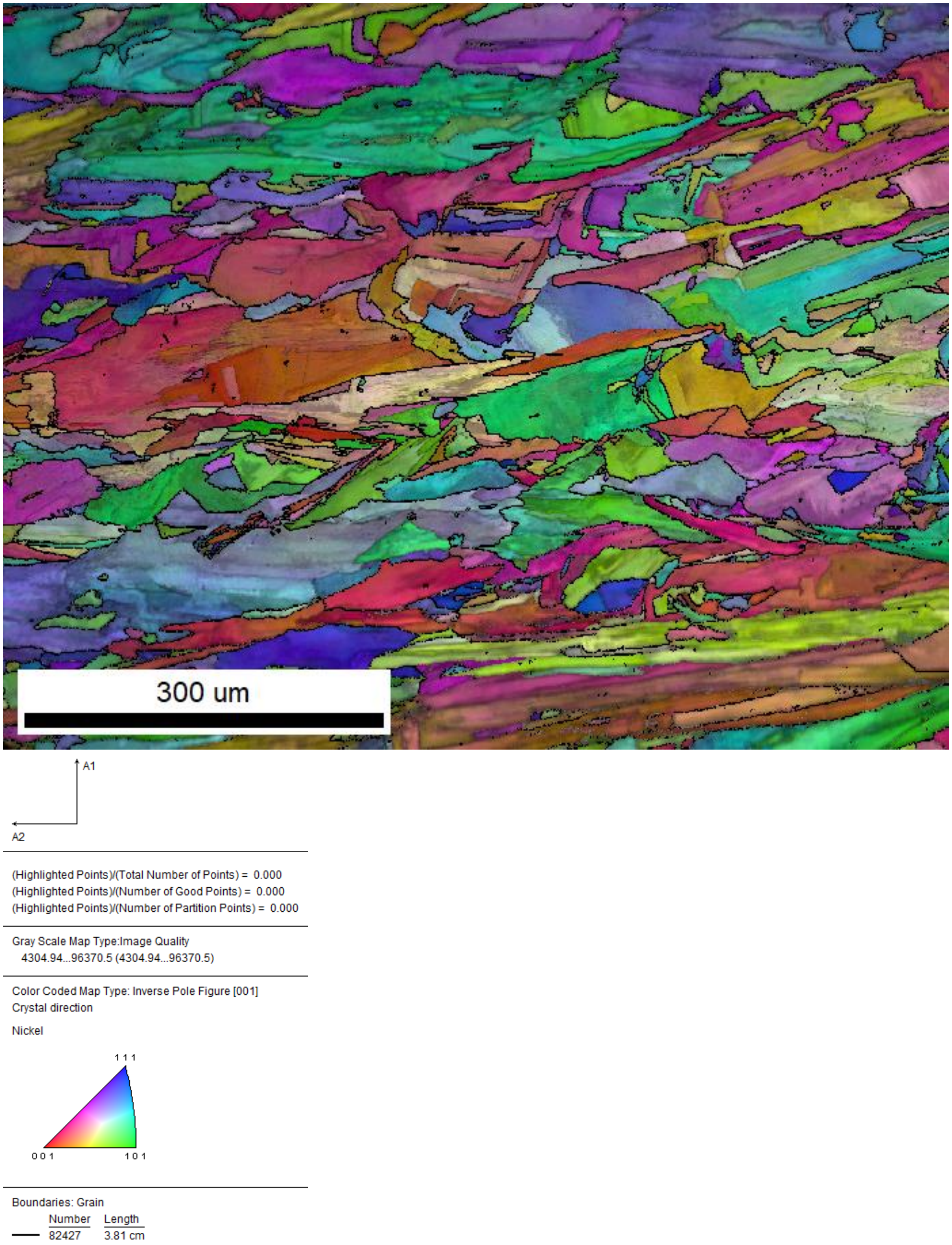

(Highlighted Points)/(Total Number of Points) = 0.000
(Highlighted Points)/(Number of Good Points) = 0.000
(Highlighted Points)/(Number of Partition Points) = 0.000

Gray Scale Map Type:Image Quality
4304.94...96370.5 (4304.94...96370.5)

Color Coded Map Type: Inverse Pole Figure [001]
Crystal direction

Nickel

Boundaries: Grain

	Number	Length
—	82427	3.81 cm

Figure 11. EBSD IPF map of as-built LPBF H282 with the build direction going toward the right.

Figure 12 shows the inverse pole figure corresponding to the EBSD map. The IPF shows that that the grains are textured with the (001) type planes parallel to the build direction, as expected. There is, however, some textural variation and not all grains conform exactly to that orientation relationship.

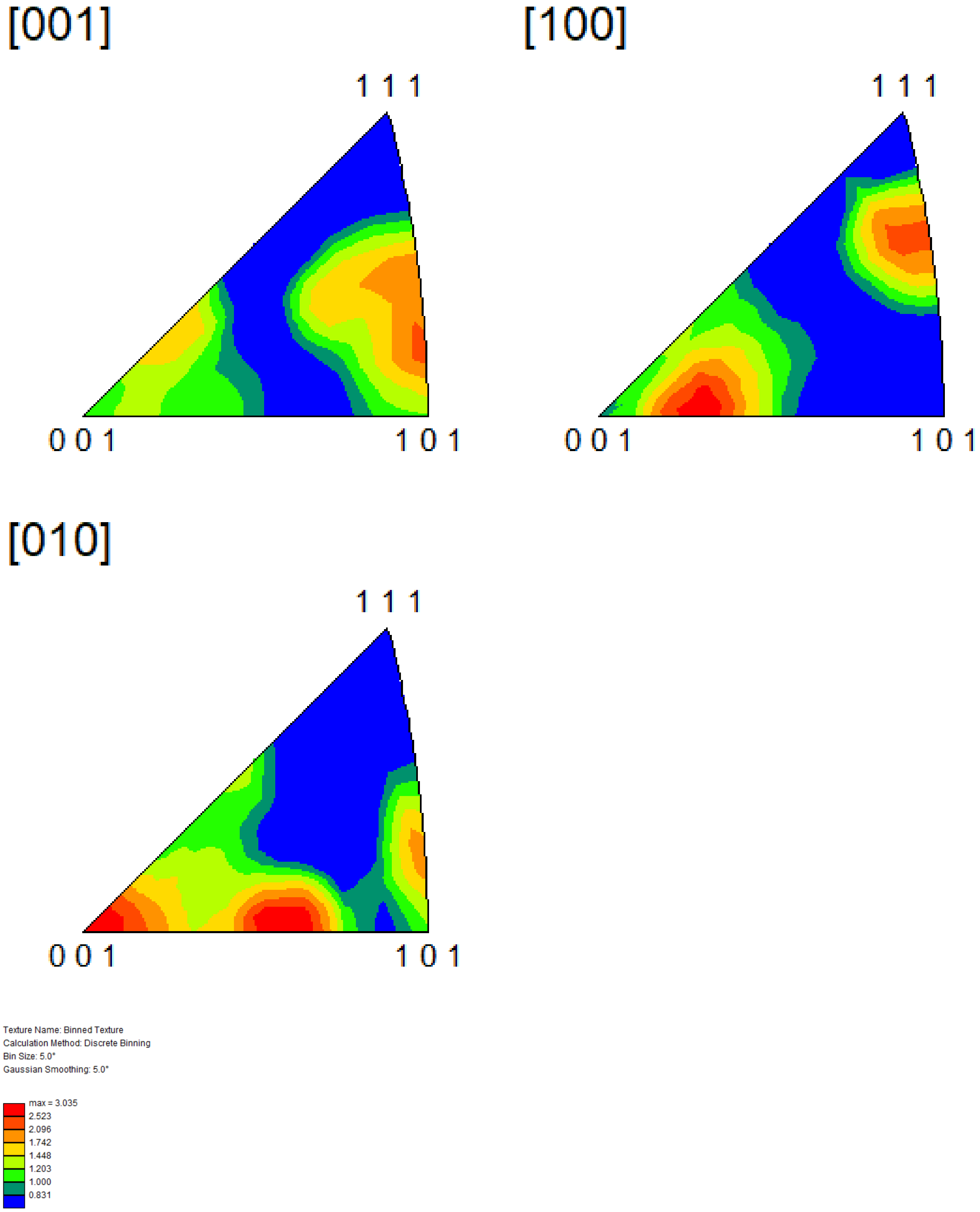

Figure 12. Integrated inverse pole figure corresponding to the same scanned area as Figure 11.

Figure 13 shows an IPF map of the sample that was heat treated at 1100 °C for 1 hour. Similar to the observations of [8-10], the figure shows that the microstructure is still elongated in the build direction and not recrystallized.

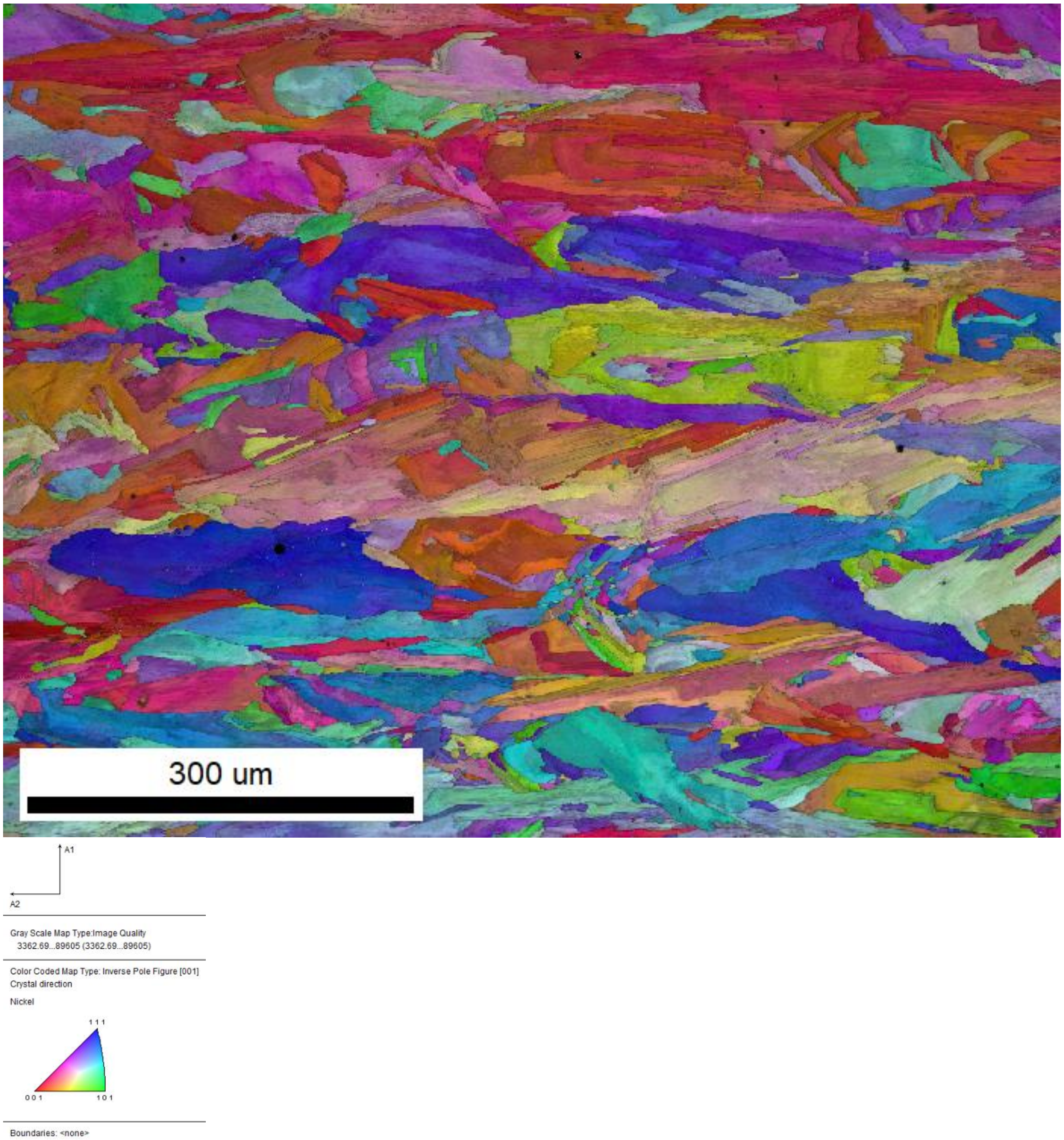

Figure 13. EBSD IPF map of LPBF H282 heat treated at 1100 °C for 1 h with the build direction going toward the right.

Figure 14 shows an IPF map of LPBF H282 after heat treatment at 1180 °C for 1 h. In this case the majority of the grains are clearly recrystallized. There are still some small areas of elongated grains, and some “hazy” grains indicating varying intragranular orientations characteristic of remnant cellular structure. Annealing twins are also visible in many grains.

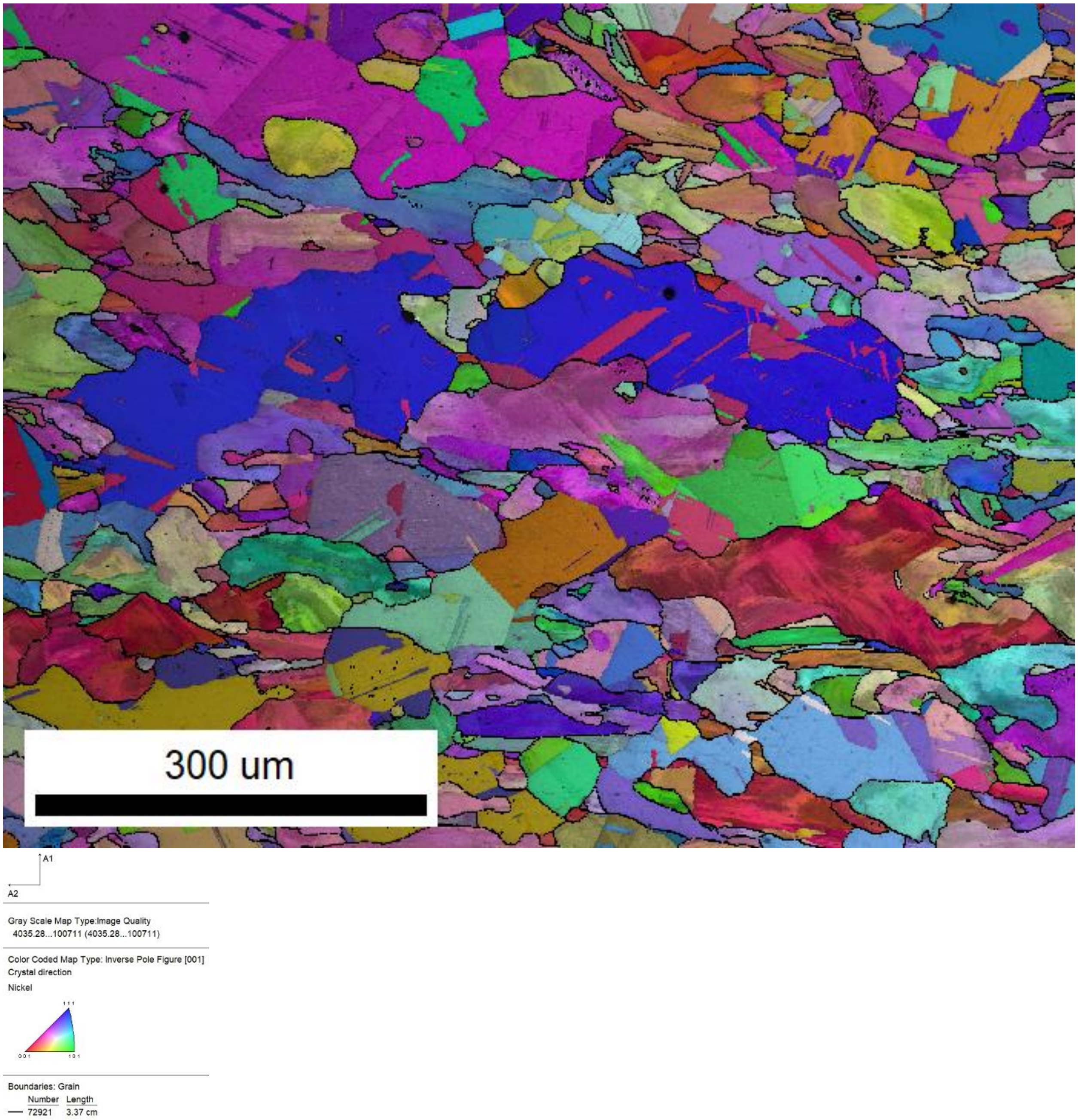

Figure 14. EBSD IPF map of LPBF H282 heat treated at 1180 °C for 1 h with the build direction going toward the right.

Figure 15 shows an EBSD IPF map of the LPBF H282 sample heat treated at 1210 °C for 2 h. The grain size is much larger than after the 1180 °C heat treatment, and much larger annealing twins are also visible. There are still a few "hazy" grains indicating remnants of the cellular structure.

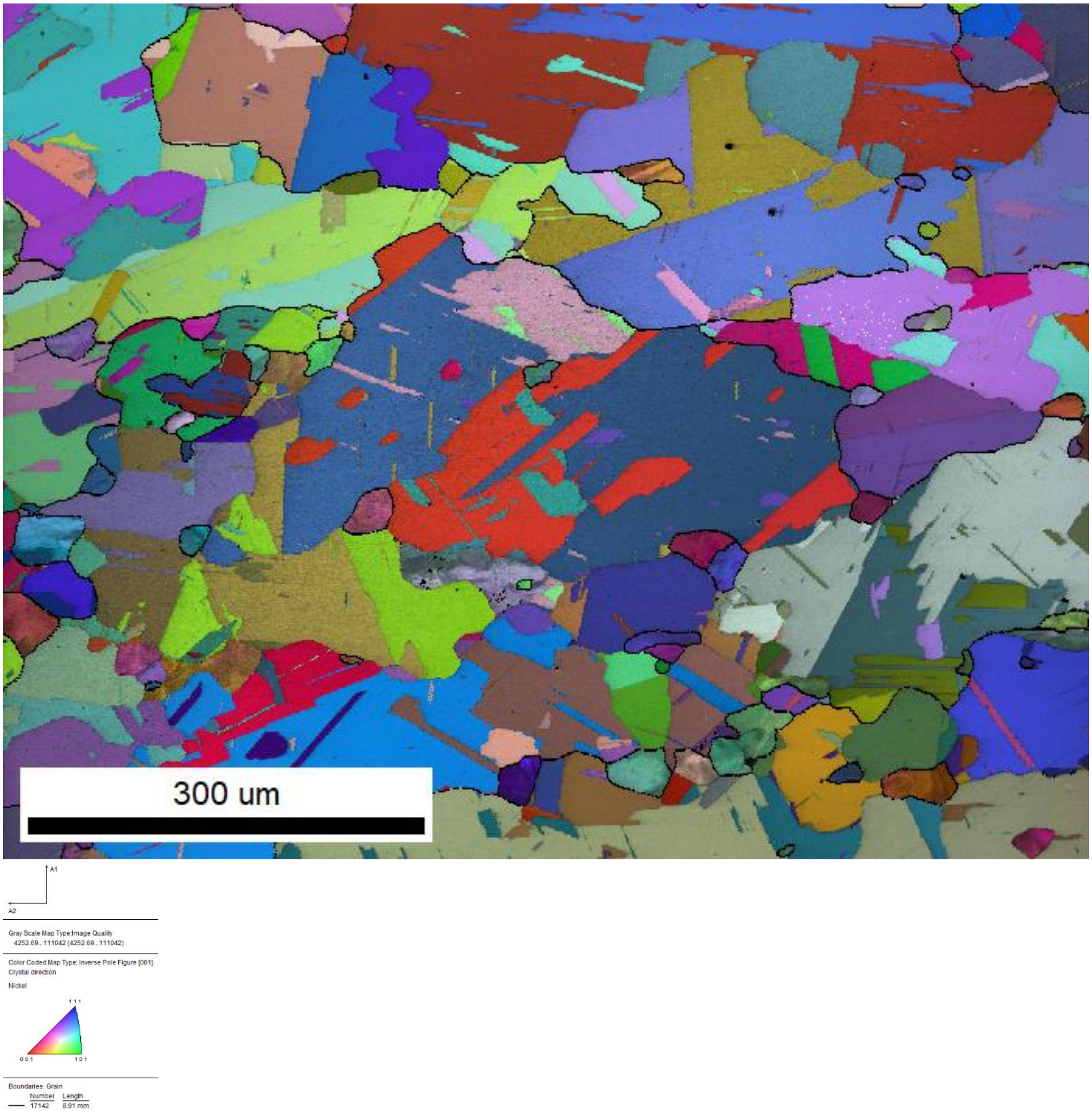

Figure 15. EBSD IPF map of LPBF H282 heat treated at 1210 °C for 2 h with the build direction going toward the right.

Figure 16 shows an EBSD IPF map of the LPBF H282 sample heat treated at 1250 °C for 2 h. The grain size is large and similar to the size of the sample heat treated at 1210 °C for 2 h. The area occupied by annealing twins appears to be larger after the 1250 °C heat treatment. A few small hazy areas, indicating remnant cellular microstructure, are present even after this heat treatment.

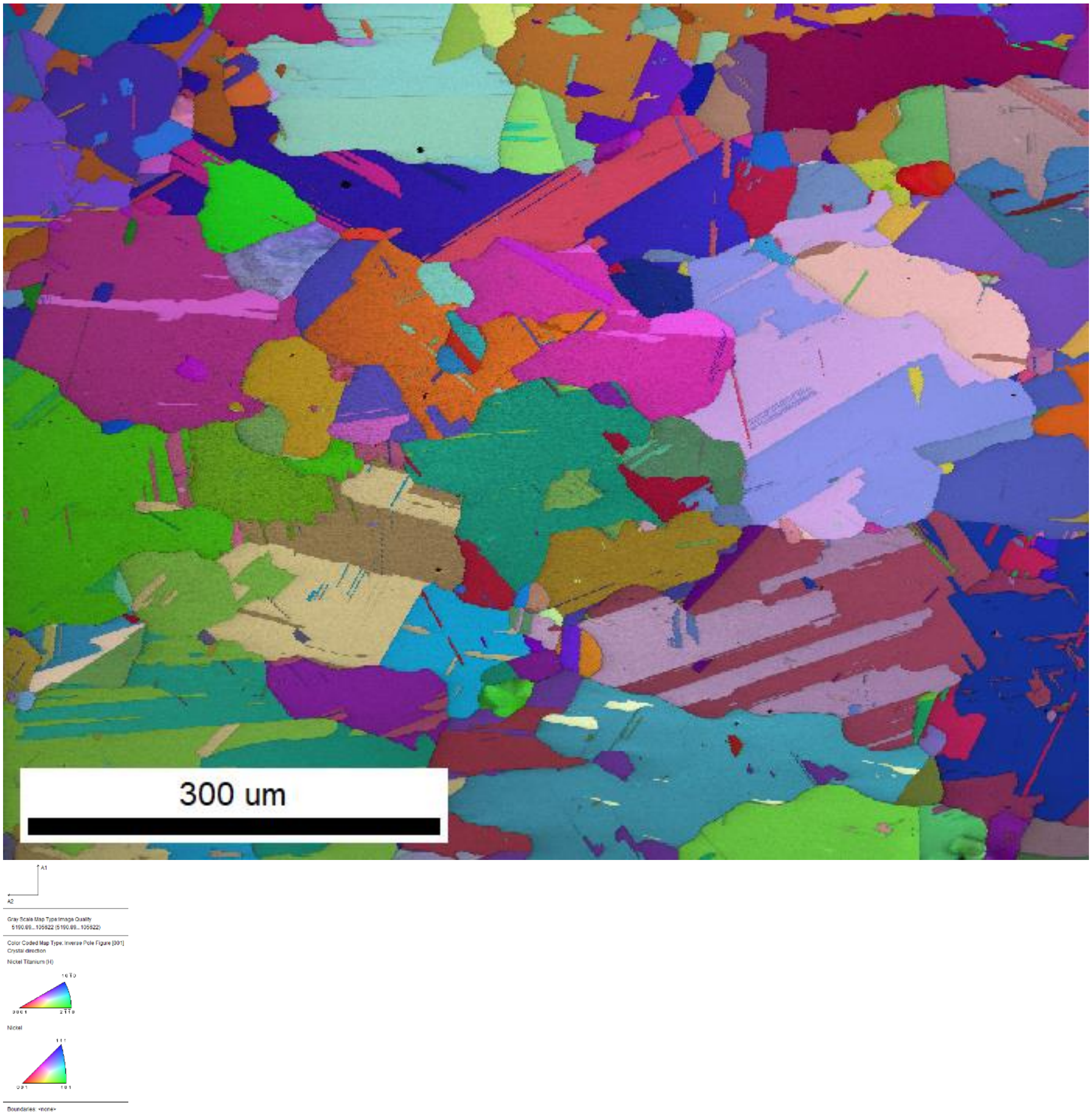

Figure 16. EBSD IPF map of LPBF H282 heat treated at 1250 °C for 2 h with the build direction going toward the right.

Figure 17 shows the average grain size calculated from the EBSD analysis. Grains are defined by 15 degrees of misorientation, and twin boundaries are excluded from the analysis. Each grain size is an average of four scans, and the area-weighted average grain diameter is used.

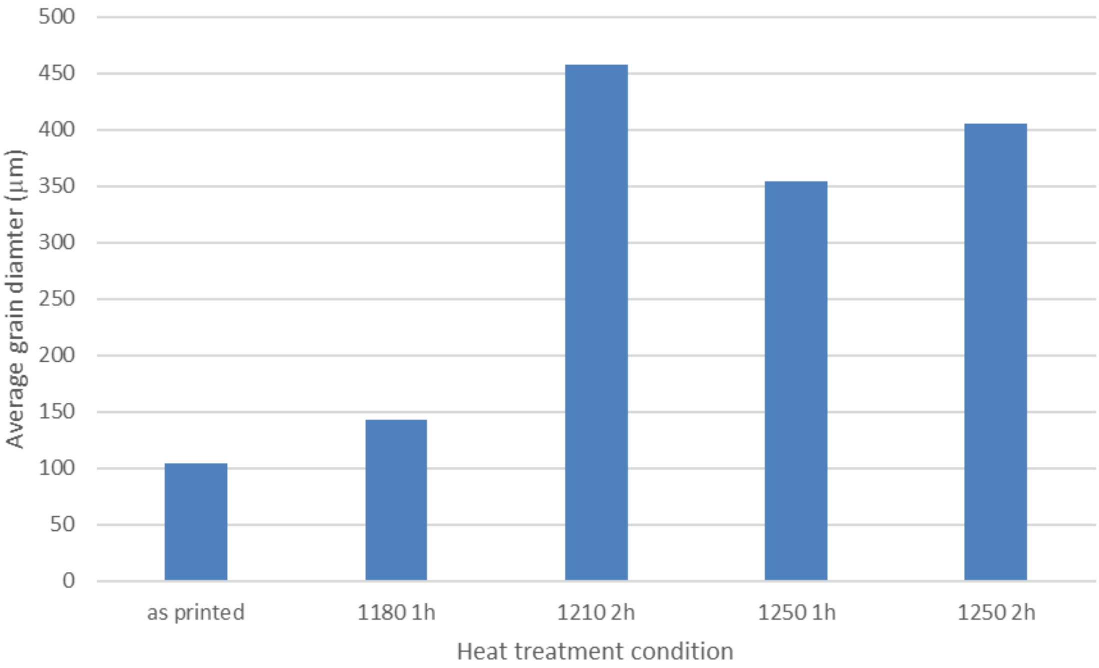

Figure 17. Average grain size calculated from EBSD scans of various heat treatments.

2.10.4 Summary

The microstructure of as-built and heat treated LPBF H282 samples from EOS was analyzed. The as-built microstructure consists of anisotropic, elongated columnar grains that are elongated in the build direction. Large areas of cellular microstructure are present inside the grains. Heat treatment at 1100 °C for 1 h does not recrystallize the microstructure, while heat treatment at 1180 °C for 1 h recrystallizes the majority of the grains. Heat treatment at 1210 and 1250 °C results in significant grain growth. The grain size at 1210 and 1250 °C are basically the same, indicating that the rate of grain growth has decreased significantly after the large grain size of ~400 µm is reached. Remnants of the cellular microstructure are present even after heat treatment at 1250 °C for 2 h. Additional work is being performed at temperatures between 1100 °C and 1180 °C, at times less than an hour to see if it is possible to get near complete recrystallization, with grain sizes between 50-100 micrometers. Grains that are too large are expected to have very poor fatigue strengths.

3. Literature Survey of Other Alloys

3.1 Scope

Other alloys is a very general term and is defined more specifically within this section. Since the study of steels, nickel-based alloys, high-entropy alloys (HEAs), refractory alloys, oxide-dispersion strengthened (ODS) alloys, and composites are all covered elsewhere in the AMMT Program, this study will focus on the materials not covered by these categories which are collectively referred to as “other” alloys. In examining other alloys, the focus was maintained on LPBF, similar to what was done with the investigation of nickel alloys. LPBF is the most industrially accepted and technologically mature AM capability, and it serves as a logical starting point to assess the characteristics of materials produced via AM. All compositions discussed in this section are reported in atomic percent (at%).

3.2 Iron-Chrome-Aluminum (FeCrAl)

Neither a steel nor an HEA, FeCrAl alloys are an attractive class of alloys developed to possess high-temperature steam oxidation resistance which were originally employed by the fossil-fuel industry and more recently have become a major area of focus in the nuclear sector as an accident-tolerant fuel cladding material [33]. Additions of chromium are made to improve intermediate-temperature oxidation resistance and mechanical strength, while aluminum additions are made to improve high-temperature oxidation, however excessive alloying of either element can induce embrittlement and weldability issues. Figure 18 qualitatively shows the variation of the oxidation and mechanical properties of FeCrAl as a function of composition. Here the idealized composition range for both part fabrication and service can be seen as being bounded by 0-20 at% chromium and 10-20 at% aluminum, though other alloying additions may adjust these relative limits.

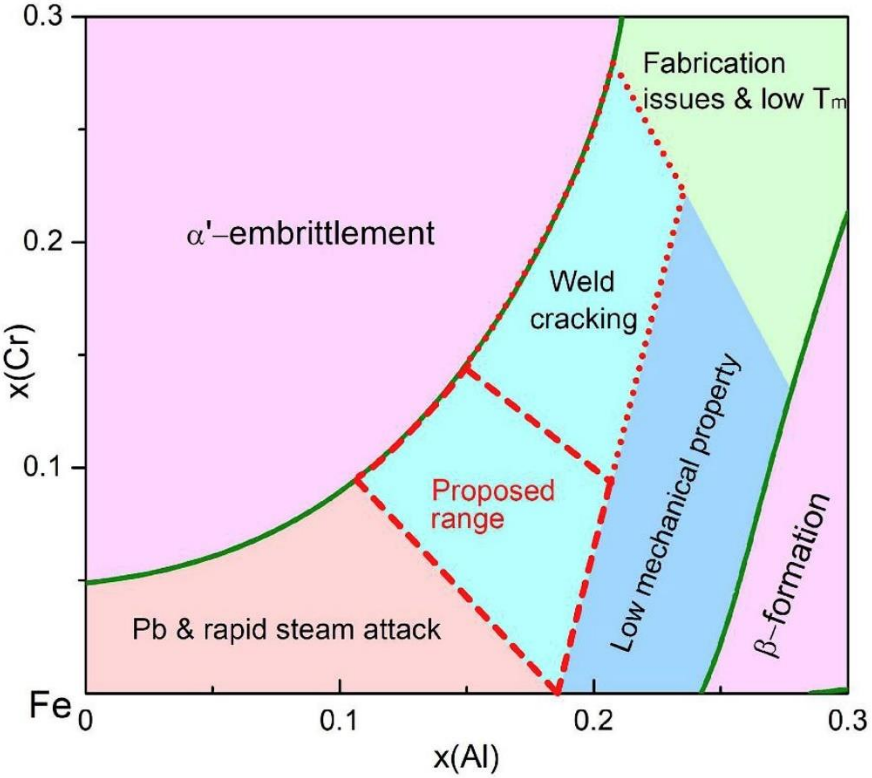

Figure 18: Map of Summary of Fe-Cr-Al composition-structure-property-performance relationships from Chang et al. [34].

Many FeCrAl alloys have been successfully produced via LPBF, including -but not limited to- 67Fe-22Cr-11Al (Kanthal AM100) [35], 75Fe-12Cr-12Al-1Mo [36], and 61Fe-20Cr-14Al-2Mo-3Ni [37], in addition to many ODS variants which fall outside this scope. A common issue with FeCrAl alloys produced via AM is solidification cracking, and solid-state cracking due to the large thermal and residual stresses associated with LPBF combined with the elevated ductile-to-brittle transition temperature (DBTT) of FeCrAl alloys relative to more conventional steels. Indeed, most commercial wrought FeCrAl alloys have been found to exhibit DBTTs ranging from ~120-320 °C, and despite often showing signs of room-temperature ductility often show minimal impact toughness at temperatures below these DBTT values [38]. Above the DBTT, impact toughness values very substantially as a function of grain size and texture, even for a single alloy composition [38], which may enable the impact toughness to be improved by optimization of print parameters for FeCrAl alloys produced via LPBF. One attractive feature of FeCrAl with regards to AM via LPBF is powder availability – due in part to previous industry uses, relatively cheap elemental constituents, and its stability in air, FeCrAl powders are more readily available and easier to handle than some other more exotic AM powders.

3.3 Zirconium (Zr) Alloys

A mainstay of the current nuclear reactor fleet, Zr alloys are used extensively in the nuclear industry as fuel cladding materials, owing primarily to their neutron transparency, though recent research thrusts have focused on alloying additions or coatings to improve their high-temperature oxidation resistance motivated by the events at the Fukushima-Daiichi generating station in 2011. In its pure form, Zr exhibits very poor corrosion resistance in aqueous environments even at modest temperatures due to in part to the poor adherence of the oxide. However, with dilute additions of Cr, Fe, tin (Sn), and niobium (Nb) totaling less than a few atomic percent, the corrosion properties can be markedly improved [39], and these dilute alloys are what are typically employed in reactors today. A major strength of Zr alloys in their inherent resistance to void swelling under typically reactor conditions, owing to the elevated rate of vacancies thermally emitted from voids which must be overcome to stabilize void formation [40]. While this lack of void swelling is an advantage over steel alloys for reactor cladding applications, the anisotropic crystal structure of Zr combined with the grain texture induced from the pilgering process to produce fuel cladding tubes can promote irradiation growth of Zr fuel cladding which is not observed in steels [41]. In stark contrast to these dilute alloy systems, Zr is also in a heavily alloyed form to produce metallic glasses, which are a class of materials shown to exhibit several promising properties including both high ductility and high strength, as well as improved corrosion resistance owing in part to their lack of grain boundaries [42]. Additionally, while still an area of active research, some Zr-based metallic glasses metallic glasses have been shown to exhibit phase stability and resistance to void swelling under both ion and neutron irradiation [43, 44].

While traditional manufacturing of Zr alloys is well established, producing Zr components via AM techniques has proven more challenging. Specifically, the high melting point and low thermal conductivity of Zr have been reported to cause melt pool instabilities during printing leading to substantial porosity and poor feature retention [45]. While no mechanical properties have been reported, fully dense and largely defect-free 99Zr-1Mo samples have been produced using LPBF within a narrow region of process parameters near a scan speed of 1050 mm^2/s and laser power densities of 53 J/mm^3 [46]. Recently, successful manufacturing of a Zircaloy-4-like alloy using LPBF has been reported with the authors reporting densities well over 99%, however, the AM processing parameter window was found to be relatively narrow and during mechanical testing the as-printed material exhibited intergranular cracking and low compressive strength, though some of this was recovered with post-build heat treatment [47]. Zr-702, a Zr alloy with up to 4.5% hafnium (Hf), has also been reported to have been successfully fabricated using LPBF with better mechanical properties and a much larger processing window than other Zr alloys [48], however, its Hf content precludes its use in most nuclear applications.

Interestingly, LPBF-produced Zr-based metallic glasses are more common in the literature than more traditional Zr-based alloys, driven in part by the biomedical industry. Zr-based metallic glasses, including 52Zr-5Ti-18Cu-15Ni-10Al [49], 59Zr-29Cu-10Al-2Nb (AMZ4) [50], 60Zr-10Fe-20Cu-10Al [51], and 58Zr-8Ni-16Cu-8Ta-10Al [52] have been used to produce parts using LPBF while remaining highly, if not fully, amorphous. While solidification cracking is not as problematic for the amorphous alloys, since there is no discontinuity between the molar volumes when going from a liquid to an amorphous solid, the amorphous Zr alloys have other unique printing challenges – namely avoiding crystallization of the metallic glass during multi-layer depositions.

Whether they are dilute crystalline alloys or heavily alloyed amorphous alloys, Zr-based powders for AM are sensitive to oxygen and nitrogen. Sufficiently fine Zr powders can pose a pyrophoric hazard making them difficult to handle safely in large quantities [53], and while LPBF is usually performed under argon, the high affinity of Zr for oxygen and nitrogen means that the Zr-based powders will more aggressively absorb these impurities from the argon cover gas when heated during printing, which may complicate efforts to recycle the powders while avoiding interstitial oxygen and nitrogen contaminants.

3.4 Titanium (Ti) Alloys

While not often used within nuclear reactor cores, Ti alloys often find use in the secondary cooling loop in the form of steam turbine blades and condenser tubes [54]. While in the United States stainless steels are often used in these applications, the growing interest in small modular reactors and mobile reactors (i.e., fission batteries) puts greater emphasis on the need to produce lightweight reactor systems and as such, Ti alloys may become more favorable for these applications. Ti is also relatively transparent to neutrons, though not as much so as Zr, making it suitable for some in-core applications, however Ti alloys generally have poor creep properties thereby limiting their in-core viability with the possible exception of niche applications such as space nuclear, where weight reduction is paramount.

Similar to Zr, Ti alloys have considerable interest in the biomedical community, however, their interest also extends to the aerospace community which has led to Ti alloys becoming one of the most studied materials systems for AM. Of the Ti alloys, 90Ti-6Al-4V (Ti64) makes up the majority of the AM literature for Ti alloys [55]. In α+β Ti alloys such as Ti64, rapid cooling rates can lead to the formation of martensitic α' lath, whose spacing is a function of the cooling rate. In LPBF, with some of the highest cooling rates of any AM process, as-printed Ti64 can feature extremely fine α' lath which leads to substantially higher tensile strength than its wrought counterpart at the cost of ductility [56]. As such, most Ti alloys produced via LPBF require post-build heat treatments to recover their ductility and produce a more traditional α+β microstructure.

Given its relatively low maximum service temperature (~300 °C), Ti64 is not particularly well suited for most nuclear applications; however, alloys such as 88Ti-6Al-2Zr-3Mo-0.3Si (TC11) and 86Ti-6Al-2Sn-4Zr-2Mo (Ti6242) have substantially higher creep strength and service temperatures (~500 °C) [57, 58], and may be more broadly applicable to use in and around nuclear reactor systems. Recently, both TC11 and Ti6242 have been produced via LPBF [59, 60], and while the as-printed materials often suffer from large residual stresses and martensite phase fractions, post-build heat treatments have been demonstrated to recover tensile ductility while still maintaining room-temperature yield strengths near 1000 MPa, as shown in Figure 19.

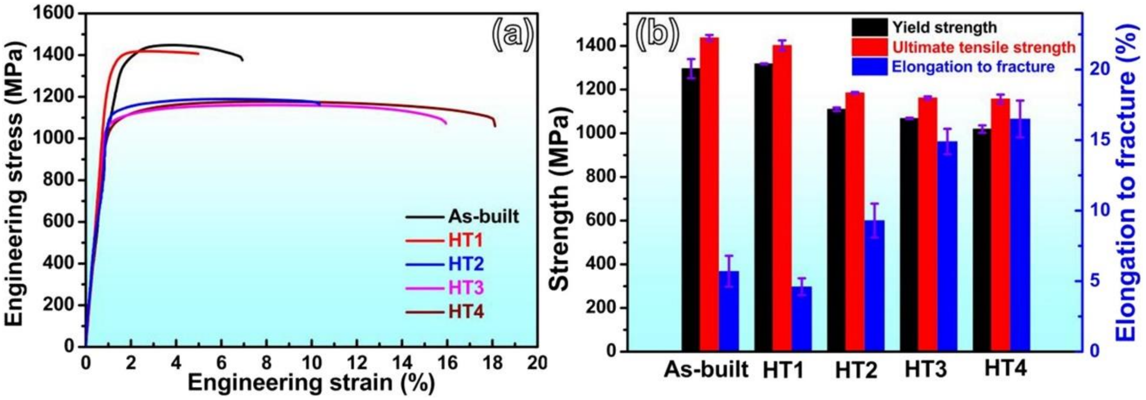

Figure 19: Effects of various heat treatments on the mechanical properties of Ti6242 produced via LPBF [60].

While most Ti alloys produced via AM require post-build heat treatments, there is a wealth of knowledge on the printing and heat treatment of AM Ti alloys provided primarily by work from the biomedical and aerospace communities. By this same token, the multi-industry interest and use of these materials provides sufficient demand to attract several large suppliers of powders which brings down the AM powder cost relative to materials with more limited applications.

3.5 Ceramics

While several AM technologies are capable of producing ceramic products (e.g., digital light processing, binder jet printing, stereolithography), most of these capabilities use polymeric compounds to bind ceramic powders together into a green body which must then be put through a series of debinding and sintering/densification heat treatments to produce the final ceramic part. Ceramic materials produced this way often undergo substantial geometric changes during the post-manufacturing heat treatments and feature microstructures and defects which differ from those that are characteristic of the LPBF process, and thus fall outside of the scope of this study. However, there have been several attempts to produce ceramic materials directly using LPBF without the use of polymeric binding compounds. While physically melting ceramic powders via laser heating to produce net shape parts is typically not viable, due to the high temperatures required, large thermal stresses induced, risk of chemical decomposition/reactions, etc., researchers have been able to produce net shape ceramic parts via LPBF by utilizing precursor materials and reactive cover gases. Specifically, using pure metal and/or oxide powders, carbides and nitrides can be produced by introducing methane or ammonia, respectively, as a cover gas during what would otherwise be conventional LPBF [61]. As a metal becomes carburized or nitrided, it typically undergoes a lattice expansion which would normally lead to substantial cracking, especially during the significant temperature transients associated with LPBF. However, while metals expand when carburized or nitrided, their oxide counterparts typically contract when reacted to form carbides or nitrides – thus by carefully tailoring the ratio of metal to oxide powders, the net volume change of the material during the carburization/nitridation should be controllable [61]. While this technique has been demonstrated to produce net shapes chromium carbide (Cr_3C_2) and chromium nitride (CrN), there are still issues of phase purity in the final product and cracking associated with the thermal stresses on cooling, however, such a technique may prove useful for producing ceramic neutron reflectors or neutron absorbers for future reactors with complex design constraints.

In addition to reactive synthesis using a cover gas as a reactant, ceramic parts can be produced via LPBF using a lower-melting-point metal to cement the ceramic particles together. For example, tungsten carbide (WC) has been produced via LPBF using titanium as a binder with densities in excess of 99%, during which a mixture of pure WC and titanium powders are used in a traditional LPBF setup [62]. Rather than directly printing the final product, LPBF has also been implemented as an intermediate step to produce net-shape ceramic preforms which can undergo further chemical processing and sintering to produce a final product. For example, complex silicon carbide and boron carbide geometries have been produced by printing porous ceramic preforms with silicon as a binder to entrain either silicon or boron carbide powder particles. By then infiltrating these ceramic preforms with a carbonaceous resin, carbonizing the resin, and sintering the part, the silicon binder can be converted into silicon carbide resulting in either a primarily silicon carbide part or a silicon carbide/boron carbide composite depending on the ceramic powders initially used [63]. As both silicon carbide and boron carbide are materials of interest within nuclear reactors, as structural components and neutron absorbers, respectively, such a manufacturing route may be of use, however, parts fabricated using these techniques often have a substantial volume fraction (>10%) of unreacted binder material in the final product, which may be deleterious given the specific application.

3.6 Ceramic Inclusions in Metal Alloys

For many metal alloys produced via laser-based AM techniques, the laser parameter processing window is often narrow, and the parameters necessary to achieve certain design constraints (e.g., sharp edges, no cracking) may produce microstructural effects that are undesirable. For example, lower laser powers may be used to prevent overbuilding, however this often results in faster local cooling rates and residual stresses in the resultant material [64]. Conversely, if one wishes to produce slower cooling rates to minimize thermal stresses they might increase the laser power, however this may then result in a more columnar/textured microstructure which has anisotropic and less-than-ideal mechanical properties [65]. This issue of cooling rate on microstructure and mechanical properties is not unique to AM, and in fact, lessons learned from metal casting can be directly applied to LPBF. Specifically, by “inoculating” the molten metal with a dispersion of fine ceramic particles, a greater density of nucleation sites is provided which can promote finer, more equiaxed grains which generally improves mechanical properties.

Introducing ceramic inclusions to promote grain refinement is categorically different from the design of ODS alloys, which fall outside the defined work scope. While ODS alloys require high densities of coherent or semi-coherent nanoscale oxide particles dispersed uniformly throughout the metal matrix, ceramic inoculants used to serve as heterogenous nucleation and can take the form of a variety of compositions and sizes, so long as interfacial energy criteria with the metal are met. Traditionally, uniformly distributing ceramic particles throughout a cast metal product is operationally difficult, since the ceramic particles often have a substantially different density than the molten metal which can cause them to either float to the top or sink to the bottom of the melt, thus requiring high-temperature stirring equipment or implementing a solid-state mechanical alloying process. In the case of LPBF, uniformly distributing ceramic particles actually may be easier than in traditional liquid-phase synthesis methods, owing to the rapid cooling rates produced during LPBF which can limit the stratification of the inoculants. To inoculate AM powders with ceramic inclusions, mixtures of the stock metal powder and the ceramic powder (typically much finer than the metal powder) can be added to a container and either agitated by hand or by aid of a mechanical agitator; alternatively, ultrasonic vibration or high-energy ball milling can be used to further mechanically alloy the ceramic particles with their metal host particles.

Much of the literature regarding ceramic inoculant additions in LPBF materials originates from the study of aluminum alloys, the mechanical properties of which have been greatly improved by a variety of ceramic inoculant additions as illustrated in Figure 20. Though aluminum alloys are not used in current nuclear reactor systems and stand to serve only an ancillary role in future lightweight nuclear systems far from the reactor core, lessons and experience from the development of ceramic-inoculated aluminum alloys via LPBF may be applied to other more nuclear-relevant alloys. For example, LPBF Inconel 718 has been produced with tungsten carbide [66], silicon carbide [67], and boron nitride [68] inoculants, all of which were shown to reduce the average grain size and improve the mechanical properties of the alloy. As such, while developing LPBF materials for nuclear applications, opportunities to improve microstructural uniformity of printed materials via the introduction of ceramic inoculants should be considered.

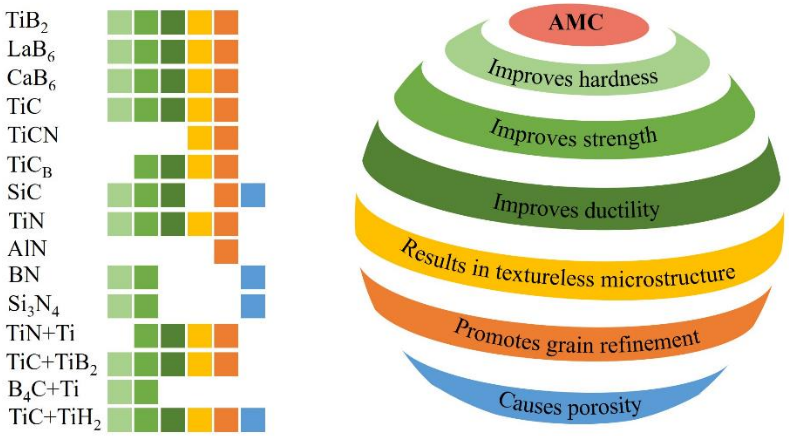

Figure 20: Summary of different ceramic inoculants used to refine additively manufactured aluminum alloys [69].

4. Conclusions

There are a number of likely useful candidates for LPBF printed nickel alloys, however, currently there is not a lot of high temperature property data available for these LPBF materials. Additionally, except in the cases of Alloys 282 and 625, the other alloys considered in this report are not readily available in powder form for use in LPBF manufacturing. Some of the alloys that are not readily available in powder form, such as Haynes 244, are still of interest due to their specialized properties (in the case of Haynes 244, the molten salt corrosion resistance). Powder availability would likely increase as the LPBF processing parameters are determined, resulting properties measured, and increased industrial interest in pursuing LPBF printed components. Additional work is planned to begin collecting high temperature properties that are either very limited, or non-existent in current reports and literature.

The recrystallization study of LPBF printed Alloy 282 has shown that it is possible to recrystallize the printed structure, which is desirable to reduce or remove the anisotropy in the mechanical properties. Currently, the 1180 °C, 1 hour recrystallization heat treatment is considered the most promising, as it resulted in a near fully recrystallized structure, and the grain size had not grown significantly. Higher temperature heat treatments results in overly large grains, which are a concern for the high temperature fatigue properties. Additional studies are ongoing to determine the feasibility of near full recrystallization with grain sizes ranging between 50-100 micrometers.

Among the different materials which fall under the designation of “other” alloys there are many promising materials which have been demonstrated to be producible via LPBF as well as opportunities for alloy development for specific nuclear applications. However, rather than ranking these materials individually in a vacuum, more context regarding specific nuclear applications is needed to evaluate the applicability of each material on a component-by-component basis, after which a determination of research and investment priority can be made. This is because, no one material is a “silver bullet” for all possible applications, and of the materials examined in this section, below are some of the general takeaways:

- The compositions of FeCrAl alloys produced via LPBF can be tailored to provide ideal mechanical and corrosion properties for nuclear reactor applications while minimizing solidification cracking during printing. However, the issue of elevated DBTTs across all LPBF-made FeCrAl alloys still persists and will likely need to be addressed to minimize solid-state cracking during cooling and subsequent room-temperature processing.
- Literature is sparce for synthesis of nuclear-grade Zr alloys manufactured via LPBF, however several research groups (predominantly from the biomedical community) have shown promising results, albeit with narrow process parameter windows. More work is needed to demonstrate the printability of Hf-free Zr alloys, though it should be noted that Zr metal powders pose additional hazards (pyrophoric) during dry handling so a specific use case would need to be provided to justify the increased operational and synthesis challenges, especially given the comparatively low cost and pre-existing supply chain for Zr alloy tubes/cladding.
- There exists a wealth of literature for the synthesis of Ti64, buoyed by support from the biomedical and aerospace industries, however the low creep strength and service temperature of Ti64 precludes its use in most nuclear systems except for some of the coolest parts of the secondary cooling loops. Other alloys with improved high-temperature creep properties have been successfully produced via LPBF, including TC11 and T6242, which may be viable for a broader range of applications, however, these will likely be limited to nuclear applications which place a major emphasis on light weighting (e.g., fission batteries, space nuclear).

- While LPBF has been used with nominal success to produce pure ceramics materials and ceramics cemented with a small volume fraction of a metallic binder, several other advanced manufacturing techniques are capable of producing ceramic components with better densities, resolutions, and mechanical integrity (i.e., without as much cracking). As such, LPBF is likely not the best tool for the job to produce ceramic materials, however, the capability to print ceramics using LPBF may be advantageous for niche applications involving multi-material systems.
- Though the majority of the research experience with introducing ceramic inoculants to refine grain structures comes from the development of aluminum alloys, much of this groundwork can be applied to the inoculation of other more nuclear-relevant alloys to reduce their texture and improve their mechanical properties when manufactured via LPBF. Introduction of such inoculants may serve to not only improve the mechanical properties of the material locally, but also produce more uniform grain structures across part geometries featuring different wall thicknesses and thermal histories.

5. References

[1] N.J. Harrison, I. Todd, K. Mumtaz, Reduction of micro-cracking in nickel superalloys processed by Selective Laser Melting: A fundamental alloy design approach, Acta Materialia, 94 (2015) 59-68.
[2] Y.B.T. Tang, C. Panwisawas, J.N. Ghoussoub, Y.L. Gong, J.W.G. Clark, A.A.N. Nemeth, D.G. McCartney, R.C. Reed, Alloys-by-design: Application to new superalloys for additive manufacturing, Acta Materialia, 202 (2021) 417-436.
[3] K.A. Mumtaz, P. Erasenthiran, N. Hopkinson, High density selective laser melting of Waspaloy (R), Journal of Materials Processing Technology, 195 (2008) 77-87.
[4] M. Salarian, H. Asgari, M. Vlasea, Pore space characteristics and corresponding effect on tensile properties of Inconel 625 fabricated via laser powder bed fusion, Mat Sci Eng a-Struct, 769 (2020).
[5] D. Tomus, P.A. Rometsch, M. Heilmaier, X.H. Wu, Effect of minor alloying elements on crack-formation characteristics of Hastelloy-X manufactured by selective laser melting, Additive Manufacturing, 16 (2017) 65-72.
[6] R. Engeli, T. Etter, S. Hovel, K. Wegener, Processability of different IN738LC powder batches by selective laser melting, Journal of Materials Processing Technology, 229 (2016) 484-491.
[7] Haynes 282 Alloy, in, Haynes International Corporation, 2021.
[8] K.A. Christofidou, H.T. Pang, W. Li, Y. Pardhi, C.N. Jones, N.G. Jones, H.J. Stone, Microstructural Control and Optimization of Haynes 282 Manufactured Through Laser Powder Bed Fusion, in: S. Tin, M. Hardy, J. Clews, J. Cormier, Q. Feng, J. Marcin, C. O'Brien, A. Suzuki (Eds.) Superalloys 2020, Springer International Publishing, 2020, pp. 1014-1023.
[9] A. Deshpande, S.D. Nath, S. Atre, K. Hsu, Effect of Post Processing Heat Treatment Routes on Microstructure and Mechanical Property Evolution of Haynes 282 Ni-Based Superalloy Fabricated with Selective Laser Melting (SLM), Metals, 10 (2020).
[10] A.S. Shaikh, F. Schulz, K. Minet-Lallemand, E. Hryha, Microstructure and mechanical properties of Haynes 282 superalloy produced by laser powder bed fusion, Mater Today Commun, 26 (2021).
[11] K. Kunze, T. Etter, J. Grasslin, V. Shklover, Texture, anisotropy in microstructure and mechanical properties of IN738LC alloy processed by selective laser melting (SLM), Mat Sci Eng a-Struct, 620 (2015) 213-222.
[12] M. Romedenne, P. Stack, R. Pillai, S. Dryepondt, Isothermal and Cyclic Oxidation of Haynes 282 Processed by Electron Beam Melting (EBM) and Laser Powder Bed Fusion (LPBF) in Dry Air at 800 and 950 degrees C, Jom-Us, 74 (2022) 1707-1718.
[13] Inconel 625, in, Special Metals Corporation, 2013.

[14] H. Wong, K. Dawson, G.A. Ravi, L. Howlett, R.O. Jones, C.J. Sutcliffe, Multi-Laser Powder Bed Fusion Benchmarking-Initial Trials with Inconel 625, International Journal of Advanced Manufacturing Technology, 105 (2019) 2891-2906.
[15] G. Marchese, M. Lorusso, S. Parizia, E. Bassini, J.W. Lee, F. Calignano, D. Manfredi, M. Terner, H.U. Hong, D. Ugues, M. Lombardi, S. Biamino, Influence of heat treatments on microstructure evolution and mechanical properties of Inconel 625 processed by laser powder bed fusion, Mat Sci Eng a-Struct, 729 (2018) 64-75.
[16] Z.H. Tian, C.Q. Zhang, D.Y. Wang, W. Liu, X.Y. Fang, D. Wellmann, Y.T. Zhao, Y.T. Tian, A Review on Laser Powder Bed Fusion of Inconel 625 Nickel-Based Alloy, Appl Sci-Basel, 10 (2020).
[17] I. Yadroitsev, M. Pavlov, P. Bertrand, I. Smurov, Mechanical properties of samples fabricated by selective laser melting, 14èmes Assises Européennes du Prototypage & Fabrication Rapide, (2009) 24-25.
[18] J. Lee, M. Terner, S. Jun, H.U. Hong, E. Copin, P. Lours, Heat treatments design for superior high-temperature tensile properties of Alloy 625 produced by selective laser melting, Mat Sci Eng a-Struct, 790 (2020).
[19] K.S. Kim, T.H. Kang, M.E. Kassner, K.T. Son, K.A. Lee, High-temperature tensile and high cycle fatigue properties of inconel 625 alloy manufactured by laser powder bed fusion, Additive Manufacturing, 35 (2020).
[20] K.T. Son, T.Q. Phan, L.E. Levine, K.S. Kim, K.A. Lee, M. Ahlfors, M.E. Kassner, The creep and fracture properties of additively manufactured inconel 625, Materialia, 15 (2021).
[21] N. Ramenatte, A. Vernouillet, S. Mathieu, A.V. Put, M. Vilasi, D. Monceau, A comparison of the high-temperature oxidation behaviour of conventional wrought and laser beam melted Inconel 625, Corrosion Science, 164 (2020).
[22] E.R. Lewis, M.P. Taylor, B. Attard, N. Cruchley, A.P.C. Morrison, M.M. Attallah, S. Cruchley, Microstructural characterisation and high-temperature oxidation of laser powder bed fusion processed Inconel 625, Materials Letters, 311 (2022).
[23] M. Andurkar, J. Gahl, B. Prorok, T. Keya, G. Harvill, S. Thompson, Effects of Build Orientation and Heat Treatment on Neutron Irradiation Hardening in Inconel 625 Fabricated via Laser Powder Bed Fusion, in: 2021 International Solid Freeform Fabrication Symposium, University of Texas at Austin, Austin, 2021.
[24] T. Keya, V. O'Donnell, J. Lieben, A. Romans, G. Harvill, M. Andurkar, J. Gahl, S.M. Thompson, B.C. Prorok, Effects of Heat Treatment and Fast Neutron Irradiation on the Microstructure and Microhardness of Inconel 625 Fabricated via Laser-Powder Bed Fusion, in: 2021 International Solid Freeform Fabrication Symposium, University of Texas at Austin, 2021.
[25] I. Cieslik, M. Duchna, T. Plocinski, E. Wyszkowska, A. Azarov, M. Zieniuk, Ion irradiation effect on the microstructure of Inconel 625 obtained by Selective Laser Melting and by the metallurgical process, Surf Coat Tech, 396 (2020).
[26] Inconel Alloy 617, in, Special Metals Corp, 2005.
[27] Haynes 244 Alloy, in, Haynes International, 2022.
[28] Haynes 233 Alloy, in, Haynes International, 2021.
[29] Inconel Alloy 740H, in, Special Metals Corporation, 2014.
[30] T.M. Smith, C.A. Kantzos, N.A. Zarkevich, B.J. Harder, M. Heczko, P.R. Gradl, A.C. Thompson, M.J. Mills, T.P. Gabb, J.W. Lawson, A 3D printable alloy designed for extreme environments, Nature, (2023).
[31] B.A. Pint, Performance of Wrought Superalloys in Extreme Environments, in: Proceedings of the 9th International Symposium on Superalloy 718 & Derivatives: Energy, Aerospace, and Industrial Applications, 2018, pp. 165-178.
[32] T. Dudziak, K. Jura, A. Polkowska, V. Deodeshmukh, M. Warmuzek, M. Witkowska, W. Ratuszek, K. Chrusciel, Steam Oxidation Resistance of Advanced Steels and Ni-Based Alloys at 700 degrees C for 1000 h, Oxid Met, 89 (2018) 755-779.

[33] Y. Yamamoto, B.A. Pint, K.A. Terrani, K.G. Field, Y. Yang, L.L. Snead, Development and property evaluation of nuclear grade wrought FeCrAl fuel cladding for light water reactors, Journal of Nuclear Materials, 467 (2015) 703-716.
[34] K. Chang, F. Meng, F. Ge, G. Zhao, S. Du, F. Huang, Theory-guided bottom-up design of the FeCrAl alloys as accident tolerant fuel cladding materials, Journal of Nuclear Materials, 516 (2019) 63-72.
[35] K.O. Gunduz, A. Visibile, M. Sattari, I. Fedorova, S. Saleem, K. Stiller, M. Halvarsson, J. Froitzheim, The effect of additive manufacturing on the initial High temperature oxidation properties of RE-containing FeCrAl alloys, Corrosion Science, 188 (2021) 109553.
[36] A.K. Hoffman, R.V. Umretiya, V.K. Gupta, M. Larsen, C. Graff, C. Perlee, P. Brennan, R. Rebak, Oxidation Resistance in 1200°C Steam of a FeCrAl Alloy Fabricated by Three Metallurgical Processes, JOM (1989), 74 (2022) 1690-1697.
[37] B. Dovgyy, M. Simonelli, M.-S. Pham, Alloy design against the solidification cracking in fusion additive manufacturing: an application to a FeCrAl alloy, Materials Research Letters, 9 (2021) 350-357.
[38] Z. Sun, Y. Yamamoto, X. Chen, Impact toughness of commercial and model FeCrAl alloys, Materials Science and Engineering: A, 734 (2018) 93-101.
[39] A.T. Motta, A. Couet, R.J. Comstock, Corrosion of Zirconium Alloys Used for Nuclear Fuel Cladding, Annual Review of Materials Research, 45 (2015) 311-343.
[40] D. Faulkner, C.H. Woo, Void swelling in zirconium, Journal of Nuclear Materials, 90 (1980) 307-316.
[41] R.B. Adamson, C.E. Coleman, M. Griffiths, Irradiation creep and growth of zirconium alloys: A critical review, Journal of Nuclear Materials, 521 (2019) 167-244.
[42] A. Inoue, Stabilization of metallic supercooled liquid and bulk amorphous alloys, Acta Materialia, 48 (2000) 279-306.
[43] T. Liu, W. Guo, M.L. Crespillo, K. Jin, Y. Zhang, H. Bei, Y. Gao, Indirectly probing the structural change in ion-irradiated Zr-Based metallic glasses from small scale mechanical tests, Intermetallics, 121 (2020) 106794.
[44] L. Yang, H.Y. Li, P.W. Wang, S.Y. Wu, G.Q. Guo, B. Liao, Q.L. Guo, X.Q. Fan, P. Huang, H.B. Lou, F.M. Guo, Q.S. Zeng, T. Sun, Y. Ren, L.Y. Chen, Structural responses of metallic glasses under neutron irradiation, Scientific Reports, 7 (2017) 16739.
[45] H. Sahasrabudhe, A. Bandyopadhyay, Laser-Based Additive Manufacturing of Zirconium, in: Applied Sciences, 2018.
[46] X. Sun, W. Zhou, K. Kikuchi, N. Nomura, A. Kawasaki, H. Doi, Y. Tsutsumi, T. Hanawa, Fabrication and Characterization of a Low Magnetic Zr-1Mo Alloy by Powder Bed Fusion Using a Fiber Laser, in: Metals, 2017.
[47] C. Song, Z. Zou, Z. Yan, X. Yao, F. Liu, Y. Yang, M. Yan, C. Han, Microstructural and mechanical property evolution of a nuclear zirconium-4 alloy fabricated via laser powder bed fusion and annealing heat treatment, Virtual and Physical Prototyping, 18 (2023) e2189597.
[48] M. Aristizabal, P. Jamshidi, A. Saboori, S.C. Cox, M.M. Attallah, Laser powder bed fusion of a Zr-alloy: Tensile properties and biocompatibility, Materials Letters, 259 (2020) 126897.
[49] X.P. Li, M.P. Roberts, S. O'Keeffe, T.B. Sercombe, Selective laser melting of Zr-based bulk metallic glasses: Processing, microstructure and mechanical properties, Materials & Design, 112 (2016) 217-226.
[50] N. Sohrabi, J. Jhabvala, G. Kurtuldu, M. Stoica, A. Parrilli, S. Berns, E. Polatidis, S. Van Petegem, S. Hugon, A. Neels, J.F. Löffler, R.E. Logé, Characterization, mechanical properties and dimensional accuracy of a Zr-based bulk metallic glass manufactured via laser powder-bed fusion, Materials & Design, 199 (2021) 109400.
[51] Y. Luo, L. Xing, Y. Jiang, R. Li, C. Lu, R. Zeng, J. Luo, P. Zhang, W. Liu, Additive Manufactured Large Zr-Based Bulk Metallic Glass Composites with Desired Deformation Ability and Corrosion Resistance, in: Materials, 2020.
[52] P. Zhang, D. Ouyang, L. Liu, Enhanced mechanical properties of 3D printed Zr-based BMG composite reinforced with Ta precipitates, Journal of Alloys and Compounds, 803 (2019) 476-483.

[53] T.D. Cooper, Review of zirconium-zircaloy pyrophoricity, in, United States, 1984.
[54] T. Allen, J. Busby, M. Meyer, D. Petti, Materials challenges for nuclear systems, Materials Today, 13 (2010) 14-23.
[55] B. Dutta, F.H. Froes, Chapter 4 - Microstructure and Mechanical Properties, in: B. Dutta, F.H. Froes (Eds.) Additive Manufacturing of Titanium Alloys, Butterworth-Heinemann, 2016, pp. 41-50.
[56] T. Voisin, N.P. Calta, S.A. Khairallah, J.-B. Forien, L. Balogh, R.W. Cunningham, A.D. Rollett, Y.M. Wang, Defects-dictated tensile properties of selective laser melted Ti-6Al-4V, Materials & Design, 158 (2018) 113-126.
[57] Y. Gu, F. Zeng, Y. Qi, C. Xia, X. Xiong, Tensile creep behavior of heat-treated TC11 titanium alloy at 450–550°C, Materials Science and Engineering: A, 575 (2013) 74-85.
[58] G.B. Viswanathan, S. Karthikeyan, R.W. Hayes, M.J. Mills, Creep behaviour of Ti-6Al-2Sn-4Zr-2Mo: II. Mechanisms of deformation, Acta Materialia, 50 (2002) 4965-4980.
[59] X. Lu, C. Shu, Z. Zheng, X. Shu, S. Chen, K. Essa, Z. Li, H. Xu, Effects of L-PBF Scanning Strategy and Sloping Angle on the Process Properties of TC11 Titanium Alloy, in: Metals, 2023.
[60] Z. Zhu, F.L. Ng, H.L. Seet, S.M.L. Nai, Tailoring the microstructure and mechanical property of laser powder bed fusion fabricated Ti–6Al–2Sn–4Zr–2Mo via heat treatment, Journal of Alloys and Compounds, 895 (2022) 162648.
[61] A.B. Peters, D. Zhang, A. Hernandez, M.C. Brupbacher, D.C. Nagle, T. Mueller, J.B. Spicer, Selective laser sintering in reactive atmospheres: Towards in-situ synthesis of net-shaped carbide and nitride ceramics, Additive Manufacturing, 45 (2021) 102052.
[62] B. Sa, S. Lu, P. Gong, D. Wang, Y. Dong, J. Cheng, G. Ren, M. Yan, Printability and properties of tungsten cemented carbide produced using laser powder bed fusion additive manufacturing with Ti as a binder, International Journal of Refractory Metals and Hard Materials, 111 (2023) 106106.
[63] S. Meyers, M. Turón Vinãs, J.-P. Kruth, J. Vleugels, B.V. Hooreweder, Laser powder bed fusion as a net-shaping method for reaction bonded SiC and B4C, Virtual and Physical Prototyping, 17 (2022) 854-863.
[64] V. Thampy, A.Y. Fong, N.P. Calta, J. Wang, A.A. Martin, P.J. Depond, A.M. Kiss, G. Guss, Q. Xing, R.T. Ott, A. van Buuren, M.F. Toney, J.N. Weker, M.J. Kramer, M.J. Matthews, C.J. Tassone, K.H. Stone, Subsurface Cooling Rates and Microstructural Response during Laser Based Metal Additive Manufacturing, Scientific Reports, 10 (2020) 1981.
[65] S. Zhang, Y. Lei, Z. Chen, P. Wei, W. Liu, S. Yao, B. Lu, Effect of Laser Energy Density on the Microstructure and Texture Evolution of Hastelloy-X Alloy Fabricated by Laser Powder Bed Fusion, Materials (Basel), 14 (2021).
[66] I.T. Ho, Y.-T. Chen, A.-C. Yeh, C.-P. Chen, K.-K. Jen, Microstructure evolution induced by inoculants during the selective laser melting of IN718, Additive Manufacturing, 21 (2018) 465-471.
[67] E. Tekoğlu, A.D. O'Brien, J. Liu, B. Wang, S. Kavak, Y. Zhang, S.Y. Kim, S. Wang, D. Ağaoğulları, W. Chen, A.J. Hart, J. Li, Strengthening additively manufactured Inconel 718 through in-situ formation of nanocarbides and silicides, Additive Manufacturing, 67 (2023) 103478.
[68] S.H. Kim, G.-H. Shin, B.-K. Kim, K.T. Kim, D.-Y. Yang, C. Aranas, J.-P. Choi, J.-H. Yu, Thermo-mechanical improvement of Inconel 718 using ex situ boron nitride-reinforced composites processed by laser powder bed fusion, Scientific Reports, 7 (2017) 14359.
[69] T. Minasyan, I. Hussainova, Laser Powder-Bed Fusion of Ceramic Particulate Reinforced Aluminum Alloys: A Review, in: Materials, 2022.